COMPUTATIONAL FLUID DYNAMICS ANALYSES OF SHIP AIR WAKES USING DETACHED-EDDY SIMULATION

S.J. Lawson, C. Crozon, F. Dehaeze, R. Steijl and G.N. Barakos

CFD Laboratory, School of Engineering
University of Liverpool, L69 3GH, U.K.
http://www.liv.ac.uk/flightscience/PROJECTS/CFD/ROTORCRAFT/RBD/index.htm
Email: crozon@liverpool.ac.uk, Florent.Dehaeze@liverpool.ac.uk, G.Barakos@liverpool.ac.uk

Abstract

This paper presents a comparative study of several Detached-Eddy Simulation closures for a ship air wake. The experiments of the National Research Council of Canada for the Simple Frigate Shape 2 are used to validate the employed Computational Fluid Dynamics method at two wind angles. The CFD results show that URANS and DES are capable of predicting the overall flow configuration. DES, however, also predicted the velocity fluctuations encountered near the ships helicopter deck. Among the assessed DES closures, the Delayed Detached Eddy-Simulation model, as well as the DDES with the Strain-Adaptive Linear Spalart-Allmaras modification did not result in substantially better predictions that the original DES formulation. The DDES SALSA resulted in flow fields very close to the DES predictions with marginal improvements. For application in helicopter ship landing, and ship wake analyses, it is therefore expected that DES and SALSA DES are the preferred simulation options. Analysis of the experimental and numerical data using Proper Orthogonal Decomposition revealed that a relatively small number of modes is needed to reconstruct the experiment. This is encouraging since efficient reduced order models of this complex flow may be possible using the POD as a meta-model. Steady-state calculation have also been conducted with an actuator disc to model the effect of the rotor, as a first attempt to study the ship/helicopter coupling problem. The results highlight the effect of the rotor on the flowfield and the importance of the coupling between ship and helicopter wakes. The calculations suggest that modelling the rotor is important and in addition, simulations should include the complete flight mechanics of the helicopter.

1 INTRODUCTION

The study of ship wakes using detailed Computational Fluid Dynamics (CFD) methods is fuelled by the need to operate vertical take-off and landing aircraft from decks on civil and military vessels. It has long been established [7] that the ship superstructure generates a highly unsteady wake coexisting with strong organised vortical structures emanating from the stern of the ship. CFD using Detached-Eddy Simulation (DES) has, in principle, the ability to simulate such flows. The predictions of the flow unsteadiness may, however, depend on the formulation of the sub-grid scale model employed in the DES and the DES formulation itself. It is therefore necessary to properly assess DES closures before routine application to ship air wakes. This assessment requires detailed experimental data. Such datasets were recently made available by the National Research Council of Canada (NRC) [12, 13] for a Simple Frigate Shape termed SFS 2. The interesting point of this investigation is that the employed hot-wire techniques provided statistics of the flow not available in previous experimental investigations. Even though the hot-wire data were not simultaneously collected at the various locations around the ship, the raw data were made available and these were used for this study.

Previous ship wake studies [6] did not provide comparisons between DES closures. This is attempted in this paper that aims to summarise the performance of the DES closures and highlights potential benefits of Delayed DES (DDES) as well as modifications of the URANS part of the model. The obtained results for two different wind directions and using five S-A models revealed a moderate sensitivity of the predictions of the velocity fluctuations on the employed closure. Interestingly, the URANS part of the model is also crucial in predicting the velocity fluctuations. Overall, the obtained mean flow data were in fair agreement with experiments, and the same holds for the fluctuations predicted by DES.

Steady-state simulations are also conducted using a $k-\omega$ turbulence model with and without an actuator disc to study the effect of the rotor downwash on the ship airwake. The SFS2 model is reused for this study as well as the Canadian Patrol Frigate (CPF) for which experimental data is also available from NRC [14, 31, 33]. The results show the importance of the downwash on the overall flowfield and assess the necessity of a good representation of the rotor effect to accurately compute the airwake. This was also simulated here with a detailed rotor on-deck simulation.

In the next paragraph, the employed CFD solver and models are presented. This is followed by a description of the CFD grids and a presentation of the obtained results. Data reduction using Proper Orthogonal Decomposition (POD) was also attempted in an effort to compress the turbulence simulation data for possible use in real time flight simulations.

2 TURBULENCE MODELS AND CFD METHODS

2.1 Spalart-Allmaras Model

The one-equation Spalart-Allmaras (S-A) turbulence model [21] solves a transport equation for the undamped eddy viscosity directly. The kinematic eddy viscosity, (ν_t), in the S-A model is calculated by:

$$\nu_t = \tilde{\nu} f_{v1} \tag{1}$$

where

$$f_{v1} = \frac{\chi^3}{\chi^3 + c_{v1}^3} \quad \text{and} \quad \chi = \frac{\tilde{\nu}}{\nu}$$

In the above equations, and hereafter, the term f refers to a function, c refers to a constant, ν is the molecular viscosity and $\tilde{\nu}$ is the undamped eddy viscosity obeying the following transport equation:

$$\begin{aligned}\frac{D\rho\tilde{\nu}}{Dt} = & \underbrace{c_{b1}\left(1 - f_{t2}\right)\tilde{S}\rho\tilde{\nu}}_{\text{Production Term}} \\ & + \underbrace{\frac{\rho}{\sigma}\left(\bigtriangledown\cdot\left(\left(\nu+\tilde{\nu}\right)\bigtriangledown\tilde{\nu}\right) + c_{b2}\left(\bigtriangledown\tilde{\nu}\right)^2\right)}_{\text{Diffusion Term}} \\ & - \underbrace{\left(c_{w1}f_w - \frac{c_{b1}}{\kappa^2}f_{t2}\right)\rho\left(\frac{\tilde{\nu}}{d}\right)^2}_{\text{Near-wall Term}}\end{aligned} \tag{2}$$

The first term on the right-hand side is the production term, the second is the diffusion term and the third is the near-wall term. The subscript b stands for *basic*, w for *wall* and t for *trip*. The parameter σ represents the turbulent Prandtl number and d is the wall-distance.

The term $\tilde{S}$ in Equation (2) is defined by the following equation:

$$\tilde{S} = S + \frac{\tilde{\nu}}{k^2 d^2} f_{v2} \quad , \qquad f_{v2} = 1 - \frac{\chi}{1 + \chi f_{v1}} \tag{3}$$

Where S is the vorticity magnitude:

$$S = \sqrt{2\Omega_{ij}\Omega_{ij}} \quad , \qquad \Omega_{ij} = \frac{1}{2}\left(\frac{\partial u_i}{\partial x_j} - \frac{\partial u_j}{\partial x_i}\right) \tag{4}$$

The function f_w in Equation (2) is given by:

$$f_w = g\left(\frac{1 + c_{w3}^6}{g^6 + c_{w3}^6}\right)^{1/6} \tag{5}$$

$$g = r + c_{w2}\left(r^6 - r\right) \quad , \qquad r = \frac{\tilde{\nu}}{\tilde{S}\kappa^2 d^2} \tag{6}$$

The f_{t2} function is defined by:

$$f_{t2} = c_{t3} \cdot e^{-c_{t4}\cdot\chi^2} \tag{7}$$

The values used for the S-A turbulence model constants are given in Table 1, with constant c_{w1} defined as:

$$c_{w1} = \frac{c_{b1}}{k^2} + \frac{\left(1 + c_{b2}\right)}{\sigma} = 3.2391 \tag{8}$$

2.2 The Strain-Adaptive Linear Spalart-Allmaras (SALSA) Model

The S-A model tends to over-predict the turbulent eddy viscosity in vortex cores. Therefore, a limiter was introduced by Rung *et al.* [18] to counter this problem. The production term is consequently modified in order to limit the turbulence production. The new production term is defined as a product of a shear stress function, the undamped viscosity and a factor C_{b1}:

$$P_{\tilde{\nu}_t} = \tilde{\nu}_t \tilde{S}_{\text{SALSA}} C_{b1} \quad , \qquad C_{b1} = 0.1355\sqrt{\Gamma} \tag{9}$$

with

$$\Gamma = \min\left[1.25, \max\left(\gamma, 0.75\right)\right] \tag{10}$$

$$\gamma = \max\left(\alpha_1, \alpha_2\right) \tag{11}$$

$$\alpha 1 = \left[1.01\left(\tilde{\nu}_t/\kappa^2 d^2 S^*\right)\right]^{0.65} \tag{12}$$

$$\alpha 2 = \max\left[0, 1 - tanh\left(\chi/68\right)\right]^{0.65} \tag{13}$$

and $\tilde{S}_{\text{SALSA}}$ the effective velocity gradient:

$$\tilde{S}_{\text{SALSA}} = S^*\left[\left(1/\chi\right) + f_{v1}\right] \tag{14}$$

where $S^* = \sqrt{2\tilde{S}_{ij}\tilde{S}_{ij}}$ with $\tilde{S}_{ij}$ representing the strain-rate tensor:

$$\tilde{S}_{ij} = \frac{1}{2}\left[\left(\frac{\partial U_i}{\partial x_j} + \frac{\partial U_j}{\partial x_i}\right)\right] - \frac{1}{3}\frac{\partial U_k}{\partial U_k}\delta_{ij} \tag{15}$$

The α_1 term allows the damping of the excessive production in high strains, while the α_2 term avoids unwanted wall damping.

2.3 Detached-Eddy Simulation (DES)

Large-Eddy Simulation (LES) is a popular tool for simulating separated turbulent flows. The philosophy behind LES is to resolve the larger, energy-containing eddies on the grid, while a sub-grid scale model is used to model the smaller, more isotropic scales. However, despite its potential, the need for fine CFD grids close to the wall does not allow the use of LES in complex flows. In these cases, Detached-Eddy Simulation may be an alternative. The main principle of DES models [23] is the use of RANS close to the walls and LES further away in the flow domain, provided substantial mesh resolution is available.

The RANS equations with a modified length scale are used in the whole domain. In the near-wall regions, the usual RANS length scale is used, whereas in the LES zones, the length scale now depends on the mesh, forcing the turbulence model to behave like sub-grid scale model used in LES. Therefore DES does not need an interface between the RANS and LES part.

Spalart introduced the mesh length scale Δ as a function of the cell size following the three directions Δ_x, Δ_y and Δ_z:

$$\Delta = \max\left(\Delta_x, \Delta_y, \Delta_z\right) \tag{16}$$

and the length scale for DES is then:

$$l_{\text{DES}} = \min\left(l_{\text{RANS}}, C_{\text{DES}}\Delta\right) \tag{17}$$

where C_{DES} is a constant. For example, in the case of the S-A model, the scale length l_{RANS} is the wall distance d. In the DES S-A model, the length scale $\tilde{d}$ is defined as:

$$\tilde{d} = \min\left(d, C_{\text{DES}}\Delta\right) \tag{18}$$

Therefore, near walls, the model will use the RANS equations, and further away, the length scale will switch to the grid length scale and the model will behave like LES.

Table 1: Closure coefficients for the S-A turbulence model.

Coefficient	c_{b1}	σ	c_{b2}	κ	c_{w2}	c_{w3}	c_{v1}	c_{t3}	c_{t4}	c_{w1}	C_{DES}
Value	0.1355	2/3	0.622	0.41	0.3	2	7.1	1.1	2	3.2391	0.78

This modification aims at increasing the dissipation term of the turbulent kinetic energy and thus decrease the production term. The dissipation term is now equal to:

$$- C_{w1} f_{w1} \left(\frac{\tilde{\nu}}{\tilde{d}} \right)^2 \tag{19}$$

2.4 Delayed Detached-Eddy Simulation (DDES)

DES may also be problematic during the transition between the LES and RANS zones. For coarse meshes around the wall, DES works as expected with a transition to LES outside the boundary layer. However, if the mesh is fine ($\Delta \simeq \delta/20$, with δ the boundary layer thickness), the simulation behaves like a Wall-Modelled LES (LES with RANS as a wall model). Problems appear for mesh sizes between these two cases, where the transition to LES takes place at about the first third of the boundary layer. Two thirds of the boundary layer are then in LES mode. This reduces the turbulent viscosity and therefore the Reynolds stresses.

To counter this, Spalart [22] developed the Delayed Detached-Eddy Simulation (DDES). DDES introduces a limiter in the length scale to ensure that transition will not take place inside the boundary layer. In the Spalart-Allmaras model, this limiter modifies the parameter r (root of the ratio between the length scale and the wall distance):

$$r_d = \frac{\nu_t + \nu}{\sqrt{\frac{\partial U_i}{\partial x_j}\frac{\partial U_i}{\partial x_j}\kappa^2 d^2}} \tag{20}$$

with κ the Kármán constant. The term $\nu_t + \nu$ can be replaced with $\tilde{\nu}$ in the S-A model. r_d equals 1 in the logarithmic part of the boundary layer and equals 0 outside the boundary layer. ν avoids this zero r_d values close to the wall. A new function f_d is also defined in Ref. [22] as:

$$f_d = 1 - \tanh\left([A r_d]^B \right) \tag{21}$$

f_d equals 1 in the LES zones and 0 elsewhere. The A and B values are arbitrary and set the shape of f_d. The values chosen to obtain correct results for a plane wall flow are [22] $A = 8$ and $B = 3$.

The new value of the length scale in the S-A model is now set at:

$$\tilde{d} = d - f_d \max\left(0, d - C_{\text{DES}}\Delta\right) \tag{22}$$

The RANS zone is defined by $f_d = 0$ and the LES zone by $f_d = 1$. In the case of highly separated flows, the detached zone is calculated in LES mode and the transition is quicker, allowing a smaller grey zone, where the model switches between the two modes. The models used in this paper and their different production terms and length scales are listed in Table 2.

2.5 CFD Method

The Helicopter Multi-Block (HMB), developed in Liverpool, is used as the CFD solver in the present paper. It solves the Navier-Stokes equations in integral form using the Arbitrary Lagrangian Eulerian (ALE) formulation for time-dependent domains with moving boundaries:

$$\frac{d}{dt}\int_{V(t)} \vec{\mathbf{w}} dV + \int_{\partial V(t)} \left(\vec{F}_i\left(\vec{\mathbf{w}}\right) - \vec{F}_v\left(\vec{\mathbf{w}}\right) \right)(\vec{n}) dS = \vec{S} \tag{23}$$

where $V(t)$ is the time dependent control volume, $\partial V(t)$ its boundary, $\vec{\mathbf{w}}$ is the vector of conserved variables $[\rho, \rho u, \rho v, \rho w, \rho E]^T$. $\vec{F}_i$ and $\vec{F}_v$ are the inviscid and viscous fluxes, including the effects of the time dependent domain. In the case of a forward flying rotor, a moving grid is used. The source term is then set at $\vec{S} = 0$ due to the lack of volume forces in the inertial frame of reference.

The Navier-Stokes equation are discretised using a cell-centered finite volume approach on a multi-block grid, leading to the following equations:

$$\frac{\partial}{\partial t}\left(\mathbf{w}_{i,j,k} V_{i,j,k}\right) = -\mathbf{R}_{i,j,k}\left(\mathbf{w}_{i,j,k}\right) \tag{24}$$

where $\mathbf{w}$ represents the cell variables and $\mathbf{R}$ the residuals. i, j and k are the cell indices and $V_{i,j,k}$ is the cell volume. Osher's [17] upwind scheme is used to discretise the convective terms and MUSCL variable interpolation is used to provide third order accuracy. The Van Albada limiter is used to reduce the oscillations near steep gradients.

Temporal integration is performed using an implicit dual-time stepping method. The linearised system is solved using the generalised conjugate gradient method with a block incomplete lower-upper (BILU) pre-conditioner. The HMB method [16, 24] has so far been used in several studies of helicopter flows and has been validated against experimental data for isolated rotors [25, 29] as well as rotor-fuselage configurations [27]. The problem of aeroelastic blades has been investigated [4, 5] as well as the implementation of harmonic balance methods [30].

Actuator discs are very simple methods that permit to account for the effect of the rotor without resolving the flow around the blades. Source terms are added to the momentum and energy equations to impose a jump of pressure across the rotor disc. This models the rotor effects without adding to the computational cost. The size, position and attitude (tilt, roll) of the rotor disc is given by the user, together with the thrust coefficient C_T^{UK} and advance ratio μ:

$$C_T^{UK} = \frac{T}{\frac{1}{2}\rho_\infty U_{tip}^2 A} \tag{25}$$

$$\mu = \frac{U_\infty}{U_{tip}} \tag{26}$$

Table 2: Comparison of the turbulence models employed.

Turbulence Model	Length Scale	Production Term
SA	d	$c_{b1}\left(1-f_{t2}\right)\tilde{S}\tilde{\nu}$
SALSA	d	$\tilde{\nu}_t\tilde{S}_{\text{SALSA}}C_{b1}$
DES	$\tilde{d}=\min\left(d, C_{\text{DES}}\Delta\right)$	$c_{b1}\left(1-f_{t2}\right)\tilde{S}\tilde{\nu}$
DES SALSA	$\tilde{d}=\min\left(d, C_{\text{DES}}\Delta\right)$	$\tilde{\nu}_t\tilde{S}_{\text{SALSA}}C_{b1}$
DDES	$\tilde{d}=d-f_d\max\left(0, d-C_{\text{DES}}\Delta\right)$	$c_{b1}\left(1-f_{t2}\right)\tilde{S}\tilde{\nu}$
DDES SALSA	$\tilde{d}=d-f_d\max\left(0, d-C_{\text{DES}}\Delta\right)$	$\tilde{\nu}_t\tilde{S}_{\text{SALSA}}C_{b1}$

For an uniform disc, the source term for the momentum equation is expressed, in dimensionless form:

$$\Delta P^* = \frac{\Delta P}{\rho_\infty U_\infty^2} = \frac{\frac{1}{2}TU_{tip}^2}{\frac{1}{2}\rho_\infty U_\infty^2 A U_{tip}^2} = \frac{1}{2}\frac{C_T}{\mu^2} \qquad (27)$$

In forward flight, the distribution of loading over the disc is not uniform and a more accurate model is required. Shaidakov [19] gave the tools to estimate the pressure jump as function of the radius and azimuth for a given advance ratio and thrust coefficient.

3 Grid Generation

A multi-block topology was generated around the SFS2 using the ICEM-CFD Hexa commercial grid generator. The grids were then converted to a format appropriate for the HMB solver. The following paragraphs detail the topologies of the employed grids for both the headwind and 45° wind test cases. Since DES computations were envisaged as well as computations at wind angles different from zero degrees, the mesh had to include the complete ship geometry.

The geometry for the SFS2 was replicated from the model used in the wind-tunnel tests [2, 32]. For the CFD computations, the geometry was non-dimensionalised by the ship length, L. The far-field boundaries for the grid were then set as $1L$ above the ship and $1.6L$ in the stream-wise and span-wise directions. An O-grid was employed around the outside and inside edges of the ship as shown in Figures 1a and 1d. Figures 1b and 1c show the surface mesh at the bow and stern of the ship, where every other grid point is plotted. Special attention had to be paid in the region near the ship hangar and landing deck. In these areas, the mesh had to be as uniform and refined as possible to capture the expected unsteady flow features that are known to cause problems during helicopter ship landing. For this reason, an almost Cartesian mesh was generated in that region. The mesh was further sub-divided into blocks to allow for efficient load-balancing of the envisaged parallel computations. The HMB solver divides blocks between processors and for this reason, a large number of blocks is bound to result in better load-balancing and code performance.

In total, the grid contained 19.2 million cells and 1446 blocks. The inner part of the landing deck had 144 cells along its length and 80 cells along the width, while the O-grid edge around the deck had 24 cells. This gave a total of 20,352 cells on the surface of the deck. The hangar was 48 cells in height, giving almost one million cells in that section of the grid alone. This mesh was almost 100% balanced for computations on up to 512 processors.

4 Results

The headwind test case was ran using the DES S-A model for 3,000 time-steps, which equates to a particle travelling three ship lengths at the free-stream velocity. For the 45° wind test case, the DES S-A model case was also ran up to 3,000 time-steps. Then, computations using the six models of Table 2 were then started from this point and ran for another 1,500 steps. The experimental data for the mean velocity components as well as for their RMS values provided by NRC of Canada [13] were then used for comparisons.

4.1 Comparisons with Experiments

The experimental data was collected using a hot-wire probe in the flow. To compare the CFD results against the experimental data, mean and RMS velocities are presented for the planes at 25%, 50%, 75% and 100% of the deck length.

The planes showing mean and RMS velocities for the headwind test case suggest that the flow behind the hangar is well predicted by the CFD. In Figure 2, the top set of planes in each sub-figure are the CFD predictions and the bottom set are the experimental measurements. The mean profiles compare favourably between the two datasets, although the stream-wise velocity in the CFD is lower where the hangar meets the deck. Also, the stream-wise velocity on either side of the deck is slightly higher in the CFD. The agreement with experiments is as good or better with other studies reported in the literature with the DES SA model [6].

Plots at 50% deck length for the 45° wind test case are shown in Figures 3 and 4. The URANS, DES and DDES models give similar predictions for the mean components. The stream-wise velocity is constantly lower across the span of the ship for the CFD compared to the experiment. However, the span-wise velocity is consistently higher. This trend has been observed in a previous study [6]. Surprisingly, normal velocity is actually better predicted on the leeward side by the URANS and DDES models than by the DES models. This is also true for other two components for the first 3 locations on the windward side.

Some discrepancies exist, however, for the RMS velocities, especially on the leeward side of the ship where the highest values occur. The URANS and DDES models under-

predicted all three components and so the solutions contained very little turbulent content. The same cannot be said for the DES models, where the span-wise and normal components were actually over-predicted compared to the experiment. Further, the stream-wise RMS component was over-predicted on the windward side of the ship, but then under-predicted on the leeward side. The restatement of the S-A model to the SALSA model seemed to have little impact on the solution, and so the remainder of the comparison will be conducted using the standard DES S-A model. The solution for this model was then ran for another 4,500 time-steps.

Planes of mean and RMS velocities for the experiment and DES S-A solution (Figure 5) highlight the differences between the two datasets and shows the comparisons are not as good as for the headwind test case. The mean stream-wise velocity seems to have a higher value towards the windward side of the deck in the experiment, whereas it is more centrally located in the CFD results. Also, the RMS values on the leeward side of the deck are not as high in the CFD. As already noted in the line plots, the span-wise mean and RMS velocities are generally higher in the CFD than in the experiment. Even with the extra run time, some of the discrepancies could be due to the differences in signal length between the two datasets.

4.2 Flow Visualisation

Contours of Q-criteria for the headwind case are shown in Figure 6. Hunt *et al.* [8] proposed the Q-Criteria to identify vortex cores and is defined as the positive second invariant of the velocity gradient tensor, ∇u, with the additional condition that the pressure must be lower than the ambient value. The second invariant Q is defined as:

$$\begin{aligned} Q &= \frac{1}{2}\left(u_{i,i}^2 - u_{i,j}u_{j,i}\right) \\ &= -\frac{1}{2}\left(u_{i,j}u_{j,i}\right) = \frac{1}{2}\left(\parallel \mathbf{\Omega} \parallel^2 + \parallel \mathbf{S} \parallel^2\right) \end{aligned} \tag{28}$$

where $\mathbf{S}$ and $\mathbf{\Omega}$ are the symmetric and anti-symmetric components of the ∇u. Thus, the Q-Criteria represents the local balance between shear strain rate and vorticity magnitude. [9]

The iso-surfaces show shedding from the top surface of the hangar close to the front face, then from the mast and finally where the flow separates from the top of the hangar at the rear face. A closer view of the landing deck shows the large vortical structures shed from the mast interacting with the smaller turbulent structures created by the flow separation, which leads to the break-up and dissipation of the larger structures.

Iso-surfaces of Q-Criteria for the 45° wind test case are shown in Figures 7 and 8 and are plotted at the same Q level as in the headwind case. Figure 7 shows four of the six models used in the study. Only large structures emanating from the front corner of the hangar and from the mast can be seen in the URANS and DDES solutions and are more characteristic of a steady flow rather than as unsteady one. The lack of small scale turbulence was due to the excessive build up of eddy-viscosity in the separated regions. Surprisingly, peak values in the separated regions were only slightly less for the DDES models than for the URANS. Only the DES models produced unsteady turbulent structures. Small vortices are seen emanating from the mast and a larger vortex from the rear corner of the hangar on the windward side of the ship.

For both the DES models, a closer view of the landing deck in shown in Figure 8, which shows the interactions of the flow separating from the side of the hangar with the flow separating from the top surface. The combined flow initially produces large vortices, which are dissipated and broken up into smaller ones after passing over the leeward side of the landing deck. The solutions for the S-A and the SALSA models are actually very similar, however, the close view also gives a better view of the shedding from the mast, which is more clearly defined in the S-A solution. The vortical structures predicted with the SALSA DES, resemble the configuration reported in [3] for the experiments. Both flow structures originating from the hangar and the bow of the ship leave a small part of the deck clear from large-scale flow unsteadiness. An area of almost triangular shape can be seen in Figure 8.

4.3 Reduced Model and POD Reconstructions

The Proper Orthogonal Decomposition (POD) is a mathematical technique used in many applications, including image processing, signal analysis and data compression [1] and aims to eliminate information which has little impact on the overall process. It was first introduced in the context of fluid mechanics and turbulence by Lumley [15] to decompose the flow into modes. These modes identify the large coherent structures which contribute to the flow. Many applications of POD use the 'method of snapshots', which was introduced by Sirovich [20] for high spatially resolved data. The 'snapshots' are taken at instances in time so that various states of the flow field are represented. A full explanation of the technique used here can be found in Lawson *et al.* [10] where the details of the employed BLAS and BLACKS libraries are also given.

In the current study, the POD is used as a form of data compression. Although the POD technique is computationally more expensive than traditional lossless methods (such as GnuZip), the elimination of some information means that it has the potential for much greater compression for very large datasets. To assess the level of compression that could be gained, data for a coarse mesh of 12,000 points was stored at every time-step in the DES S-A 45° wind simulation. The POD was then applied to the data to obtain the reduced order model. The eigenvalues from the decomposition are representative of the amount of energy stored in each mode of the flow. A nominal criterion, given by Sirovich [20], is that the number of modes retained should be equivalent to 99% of the sum of the eigenvalues. Figure 9 shows the cumulative energy for increasing modes for the velocity components. Here, the 99% level is attained after approximately 350 modes,

The stream-wise and span-wise velocity time signal at a point in the wake region behind the hangar was reconstructed using 10, 100 and 350 POD modes (Figure 10). The first reconstruction using 10 modes only captures the low frequency oscillations of the signal and so has discarded too much information to recreate the high frequency part. An increase to 100 modes captures the overall signal to a much greater extent, since much of the high frequency oscillation are also

captured in both velocity components. Therefore, for applications where the very high frequency part is less important, storing 100 modes would be sufficient. Finally, when using 350 modes (as suggested by the values of the eigenvalues), the reconstructed signals are almost identical to the original signals.

To further highlight the effect in the flow-fields of discarding some flow information, planes of RMS stream-wise and span-wise velocity are shown in Figure 11 for 10 and 100 modes. On each plot, the bottom set of planes are the original CFD results and the top set are the reconstructions. The reconstructions using 10 modes are not too different from the original at the locations where the RMS velocity is low, such as on the windward side of the ship. However, there are very large differences on the leeward side where the RMS is high. As shown in the time signals, using 100 modes recreates the flow to a good level of accuracy overall. There are few locations where the flow differs, for example in the stream-wise velocity, the main difference is in the plane closest to the hangar on the leeward side, where the RMS is not quite as high as in the original flow-field.

The results shown provide evidence that the POD technique can be used to reduce the amount of data stored without significant implications on the reconstructed flow-fields. Table 3 compares the data storage needed for this test case and the reduction that is obtained using GnuZip lossless compression and using the POD technique. For this reduced dataset, the original dataset size was 636 MB. If these are simply compressed using a lossless compression program, such as the GnuZip method, then this reduced by 24%. Note that all files are stored in Binary format and so the reduction would be greater if stored in ASCII.

The POD code produced two types of files: the spatial modes and the temporal modes, where each spatial mode is the same size as one of the original flow-fields. Therefore, if all modes were needed, then the amount of data actually increases and the method would not be suitable. However, since only 350 modes were needed to achieve 99% of the energy, then the amount of data reduced to 189 MB and was equal to a 70% reduction. Further, this data can also then be compressed using GnuZip, which then reduced it to 121 MB. This gives a final figure of 81% reduction in data storage.

Although the method was only performed on a small dataset, it demonstrates the potential of the method for use with very large datasets and could be a candidate for efficient storage in the future.

4.4 Effects of the Rotor Disc

Two rotor models using actuator disc methods were added to the CPF and steady-state calculations were conducted with a $k-\omega$ turbulence model. The values of the thrust coefficient, advance ratio, position and attitude of the rotor disc reproduce those of the experiments from Zan [31] and are presented in Table 4. The thrust coefficient was the one measured in still air and μ corresponds to the experiments conducted with a wind velocity of 19m/s. The rotor disc was centered on the landing deck with no tilt and roll angle.

Figure 12 shows the values for the streamwise and spanwise velocities on a set of planes and highlights the important effect of the downwash on the overall flowfield. The trace of the boat superstructure is less visible as has been mixed with the rotor downwash, with the combined wake expanding further laterally due to the effect of the ground, forming two large vortices between the rotor and the deck.

The presence of the hangar confines the flow and the recirculation zone moves further downstream and increases in size. The contours of streamwise velocity and the streamlines are shown figure 13, the actuator disc is represented by the horizontal black line above the deck.

To quantify the effect of the boat wake on the rotor, the distribution of downwash (Z-axis velocity) is plotted in Figure 14 for both both headwind and 45° sidewind, with and without actuator discs. The recirculation behind the hangar creates a zone of upwash in front of the rotor disc and the downwash is reduced compared to the rear part. For a 45° sidewind, a large vortex rolls over the flight deck, creating an asymmetric distribution of downwash. The intensity of this vortex is sufficient to create strong changes in helicopter attitude when approaching the deck. Moreover, the use of a non-uniform actuator disc produces a different flow pattern, an accurate prediction of the rotor aerodynamics is therefore necessary to predict accurately the flowfield and this is explained in the next paragraph.

4.5 CFD of the Full Ship-Helicopter Interaction

Given the difficulty to gather experimental data from at-sea trials or perform wind-tunnel experiments at realistic Reynolds and Mach number, the CFD methods appear as an easier way to study ship/helicopter interactions. However, they are limited by the increased computational cost due to the problem complexity and the variety of time scales found in the flow.

A full CFD simulation of Ship/Helicopter interaction has been conducted previously [11] using a realistic Type-23 frigate geometry and a detailed Sea-King helicopter model with articulated main and tail rotors. The different elements of the grid are put together using a sliding plane method implemented in HMB [26], to allow relative rigid-body motions and non-matching mesh. The blades are articulated and include trailing edge flaps, using a grid deformation method [28, 29]. Figure 15 shows 2 views of the multi-block structured grids employed. The total computational domain contains around 103 millions cells and such a computation is hard to obtain using the local cluster at Liverpool, especially because of the very small time stepping necessary to compute the flow around the rotor. The HECToR facility was used to perform two cases: headwind and 30 degrees sidewind, with the helicopter fixed over the deck.

The contours of pressure are shown Figure 16 and clearly show the stagnation areas and pressure distribution on the suction side of the blades. No discontinuities were found in the solution, despites the complexity of the calculation and the use of non-matching grids and deformable grids. This test case demonstrated the ability of HMB to cope with complex cases, including multiple sliding planes, articulated rotors with flaps, flows with a variety of speed scales, efficient parallel computation.

Figure 17 shows the loads on the rotor as normal force

Table 3: Size of flow-field and POD datasets for the SFS2 and the percentage reduction over the flow-fields dataset.

	Size(MB)	**Reduction (%)**
All Flow-fields (1532 Files)	636	
GnuZip Compressed Flow-field Files	482	24.2
Spatial POD Modes (all modes)	636	
Temporal POD Modes (all modes)	191	
Total POD Modes (all modes)	827	-27.8
GnuZip POD Modes (all modes)	530	16.7
Spatial POD Modes (350 modes)	145	
Temporal POD Modes (350 modes)	44	
Total POD Modes (350 modes)	189	70.3
GnuZip POD Modes (350 modes)	121	81.0

Table 4: Parameters used for the actuator disc calculations

C_T^{UK}	μ	Altitude above deck	Wind angle	Tilt	roll
0.00734	0.118	9m	0° and 45°	0°	0°

and moment coefficients around the azimuth. It is interesting that the normal force coefficient on the disk is low at the front and this is apparently due to the inflow the rotor sees at this configuration due to the ship super-structure. The rotor appears to have high loading at the rear and moderate loading on both the advancing and retreating sides. This is different to the typical rotor flight where most of the load is carried by the front and back of the disk. The situation on the moment is different since it is influenced by the flap actuation. The rotor has five blades and the actuation of the flaps followed a five per revolution pattern. Consequently, the minima and maxima of the moment follow the same pattern. This is certainly a first look with CFD at this complex problem and clearly a set of computations at different conditions would be desirable for the complete picture to emerge as to how flaps influence the loads and what is the effect of the wake on the rotor. The need for HPC to be applied for this case is also strengthened by the lack of experiments for such realistic helicopter/ship cases.

5 Conclusions and Future Steps

In this work, several DES models were assessed for flows pertinent to helicopter ship landing. The experiments of the NRC of Canada for the wake of a simplified ship design (SFS2) were used and compared against CFD. It was found that all models including URANS were able to capture the main flow characteristics for a zero degree headwind case and for 45 degree leeward configuration. The velocity RMS values, were better predicted by the DES models, with URANS underestimating the RMS values. The DES predictions were not perfect but captured most of the flow unsteadiness and the main flow structures over the ship hangar and landing deck. The use of the DDES formulation did not result in improvements for this case, apparently due to the already fine and near-Cartesian grids employed for computations for this relatively simple ship shape. The SALSA modifications used in conjunction with SA model offered similar results to the original DES-SA formulation with marginally better results for the peak of the RMS values near the 50% deck height in the middle of the helicopter deck. The comparisons for this complex flow case are, however, encouraging suggesting that DES is a good method for predicting data for ship wakes. The vast amount of data generated using the DES approach were compressed using Proper Orthogonal Decomposition and their size was dramatically reduced. the POD approach allows for these data to be stored and re-used for further analysis and/or potential application to helicopter ship landing simulation. About 100 modes were adequate to reconstruct the overall signal with its main frequencies. Increasing the modes to 350 results in almost perfect match between the original and the re-constructed signals.

Although steady RANS methods are not adapted for such unsteady flows, the results on the CPF model with actuator disc show that the ship airwake is likely to affect the helicopter flight, especially for sidewinds. The rotor downwash also modifies the overall flow topology, therefore coupling the ship and rotor aerodynamics. This highlights the importance of performing coupled calculations for the study of rotors in ship airwakes. As a demonstration case, the steady aircraft was simulated during landing on a Type-23 frigate. The results show the complexity of the case and highlight the required CPU cost for such calculations.

In the future, this work is directed towards CFD simulation of a rotor above the deck and validation of the DES approach for this even more complex flow case. Pilot and flight mechanics models are also to consider along with the coupled simulations.

ACKNOWLEDGMENT

The financial support of AgustaWestland to the AgustaWestland Liverpool Advanced Rotorcraft Center (AWLARC) is gratefully acknowledged.

REFERENCES

[1] G. Berkooz, P. Holmes, and J.L. Lumley. The Proper Orthogonal Decomposition in the Analysis of Turbulent Flows. *Annual Review of Fluid Mechanics*, 25:539–575, 1993.

[2] B.T. Cheney and S.J. Zan. Cfd code validation data and flow topology for tccp aer-tp-2 simple frigate shape. *Ottawa, Canada*, 1999.

[3] B.T. Cheney and S.J. Zan. Cfd code validation data and flow topology for the technical co-operation program aer-tp2 simple frigate shape. In *Technical REport LTR-A-035*, pages NRC–CNRC, Canada, April 1999.

[4] F. Dehaeze and G.N. Barakos. Hovering rotor computations using an aeroelastic blade model. *Royal Aeronautical Society*, 116(1180), 2012.

[5] F. Dehaeze and G.N. Barakos. Mesh deformation method for rotor flows. *Journal of Aircraft*, 49(1):82–92, 2012. cited By (since 1996) 0.

[6] J.S. Forrest and I. Owen. An Investigation of Ship Airwakes using Detached-Eddy Simulation. *Computers and Fluids*, 39(4):656–673, April 2010. doi:10.1016/j.compfluid.2009.11.002.

[7] J. Val. Healey. The Aerodynamics of Ship Superstructures. In *AGARD Conference Proceedings 509, Aircraft Ship Operations: Papers presented at the Flight Mechanics Panel Symposium, Seville, Spain, 20th-23rd May*, pages 4.1–4.14, November 1991.

[8] J.C.R Hunt, A.A. Wray, and P. Moin. Eddies, Streams and Convergence Zones in Turbulent Flows. *Center for Turbulence Research, Proceedings of the Summer Program*, (N89-24555):193–207, 1988.

[9] J. Jeong and F. Hussain. On the Identification of a Vortex. *Journal of Fluid Mechanics*, 285:69–94, 1995.

[10] S.J. Lawson, G.N. Barakos, and A. Simpson. Understanding Cavity Flows using Proper Orthogonal Decomposition and Signal Processing. *Journal of Algorithms and Computational Technology*, 4(1):47–70, March 2010. doi: 10.1260/1748-3018.4.1.47.

[11] SJ Lawson, M. Woodgate, R. Steijl, and GN Barakos. High performance computing for challenging problems in computational fluid dynamics. *Progress in Aerospace Sciences*, 2012.

[12] R.G. Lee. TTCP AER TP2 Dynamic Interface Workshop. In *SFS 2 Code Validation Data Update*, April 2003. Patuxent River, USA.

[13] R.G. Lee and S. Zan. Wind Tunnel Testing of a Helicopter and Rotor in a Ship Airwake. *Journal of the American Helicopter Society*, 50(4):326–337, 2005.

[14] R.G. Lee and S.J. Zan. Wind tunnel testing of a helicopter fuselage and rotor in a ship airwake. *Journal of the American Helicopter Society*, 50:326, 2005.

[15] J.L. Lumley. *Stochastic Tools in Turbulence*, volume 12 of *Applied Mathematics and Mechanics, An International Series of Monographs*. Academic Press, 1970.

[16] R. Morvant, K.J. Badcock, G.N. Barakos, and B.E. Richards. Aerofoil-Vortex Interaction Using the Compressible Vorticity Confinement Method. *AIAA Journal*, 43(1):63–75, 2004.

[17] S. Osher and S. Chakravarthy. Upwind Schemes and Boundary Conditions with Applications to Euler Equations in General Geometries. *Journal of Computational Physics*, 50:447–481, 1983.

[18] T. Rung, U. Bunge, M. Schatz, and F. Thiele. Restatement of the Spalart-Allmaras Eddy-Viscosity Model in Strain-Adaptive Formulation. *AIAA Journal*, 41(7):1396–1399, July 2003.

[19] V I Shaidakov. Disk vortex theory of main rotor with constant loading on the disk. *Helicopters Design Aerodynamics*, 381, 1976.

[20] L. Sirovich. Turbulence and the Dynamics of Coherent Structures. *Quarterly of Applied Mathematics*, 3:561–590, 1987.

[21] P.R. Spalart and S.R. Allmaras. A One-Equation Turbulence Model for Aerodynamic Flows. *La Recherche Aerospatiale*, 1:5–1, 1994. Also paper AIAA-1992-0439.

[22] P.R. Spalart, S. Deck, M.L. Shur, K.D. Squires, M.Kh. Strelets, and A. Travin. A New Version of Detached-Eddy Simulation, Resistant to Ambiguous Grid Densities. *Theoretical Computing Fluid Dynamics*, 20:181–195, May 2006. doi:10.1007/s00162-006-0015-0.

[23] P.R. Spalart, W-H. Jou, M. Strelets, and S.R. Allmaras. Comments on the Feasibility of LES for Wings, and on a Hybrid RANS/LES Approach. In *Proceedings of the 1st AFOSR International Conference On DNS/LES, Columbus, OH, August 4–8*, 1997.

[24] A. Spentzos, G. Barakos, K. Badcock, B.E. Richards, P. Wernert, S. Schreck, and M. Raffel. CFD Investigation of 2D and 3D Dynamic Stall. *AIAA Journal*, 34(5):1023–1033, 2005.

[25] R. Steijl and G.N. Barakos. A Computational Study of the Advancing Side Lift Phase Problem. *Journal of Aircraft*, 45(1):246–257, 2008.

[26] R. Steijl and G.N. Barakos. Sliding Mesh Algorithm for CFD Analysis of Helicopter Roto-Fuselage Aerodynamics. *Int. J. Numer. Meth. Fluids*, 58:527–549, 2008.

[27] R. Steijl and G.N. Barakos. Cfd analysis of complete helicopter configurations - lessons learnt from the goahead project. *Aerospace Science and Technology*, 19(1):58–71, 2012. cited By (since 1996) 0.

[28] R. Steijl and G.N. Barakos. An efficient cfd method for analysis of flapped rotor blade sections. *submitted to Journal Of Aircraft*, 2012.

[29] R. Steijl, G.N. Barakos, and K.J. Badcock. A Framework for CFD Analysis of Helicopter Rotors in Hover and Forward Flight. *Int. J. Numer. Meth. Fluids*, 51:819–847, 2006.

[30] M.A. Woodgate and G.N. Barakos. Implicit computational fluid dynamics methods for fast analysis of rotor flows. *AIAA Journal*, 50(6):1217–1244, 2012. cited By (since 1996) 0.

[31] S. J. Zan. Experimental determination of rotor thrust in a ship airwake. *Journal of the American Helicopter Society*, 47, 2002.

[32] S.J. Zan. Surface flow topology for a simple frigate shape. *Canadian Aeronautics and Space Journal*, 47(1):33–43, 2001.

[33] S.J. Zan, G.F. Syms, and B.T. Cheney. Analysis of patrol frigate air wakes. In *RTO applied vehicle technology panel symposium*, pages 7–1, 1999.

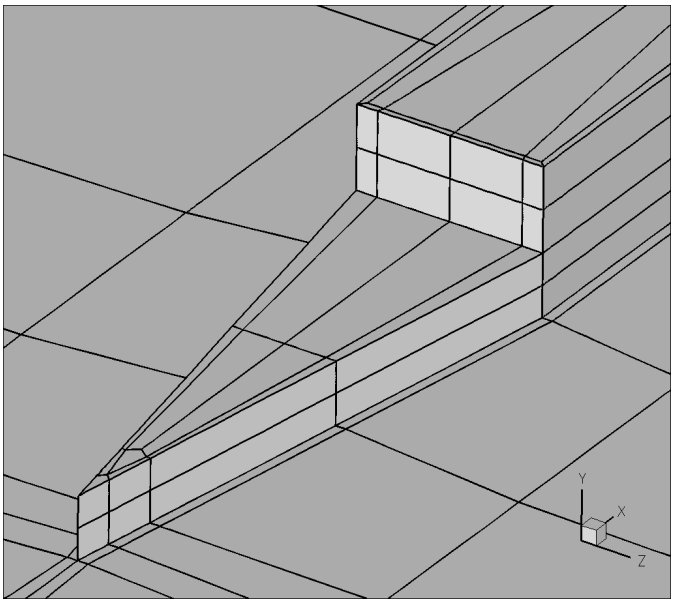

(a) Surface Blocking at Bow

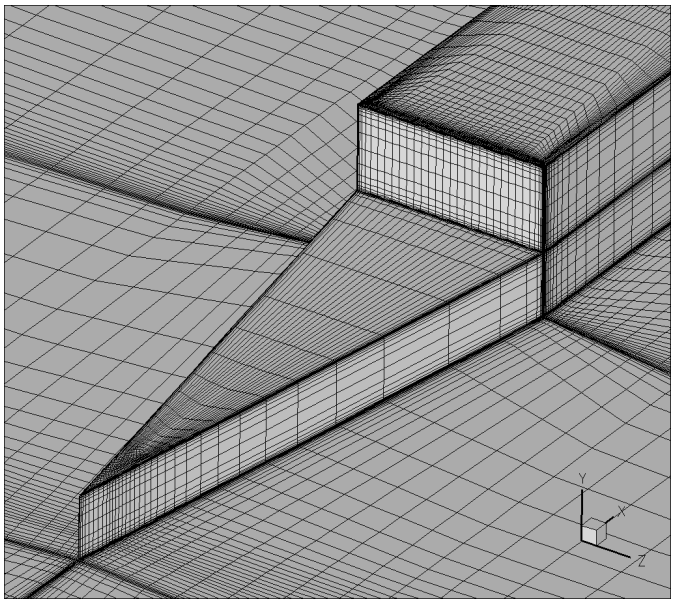

(b) Surface Mesh at Bow

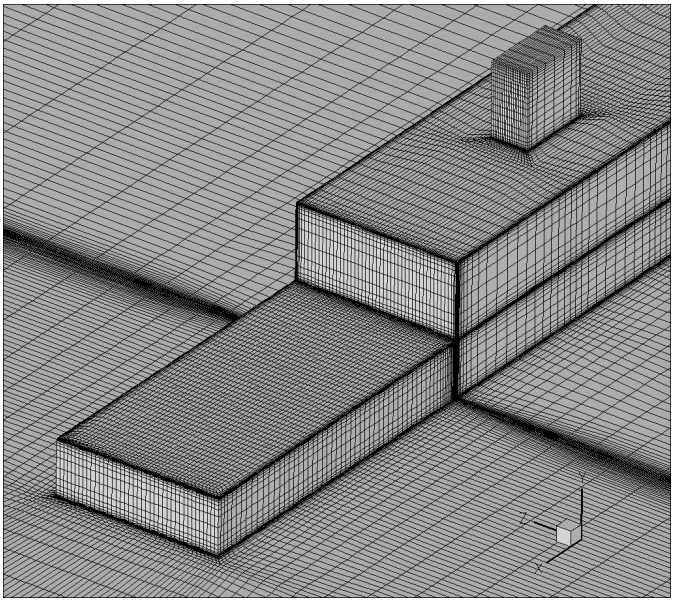

(c) Surface Mesh at Stern

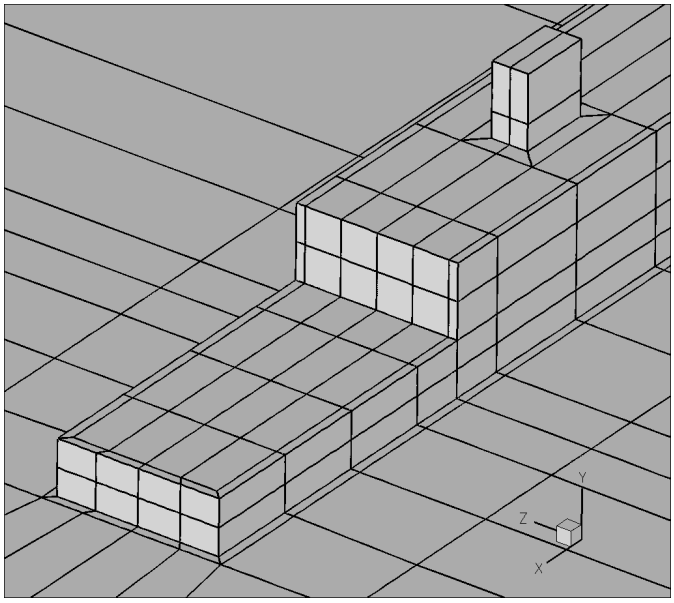

(d) Surface Blocking at Stern

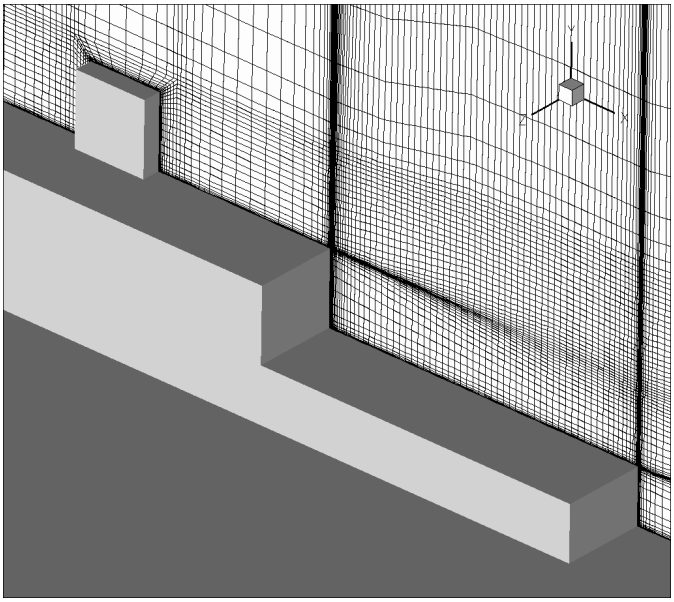

(e) Slice of Volume Mesh in Z-direction

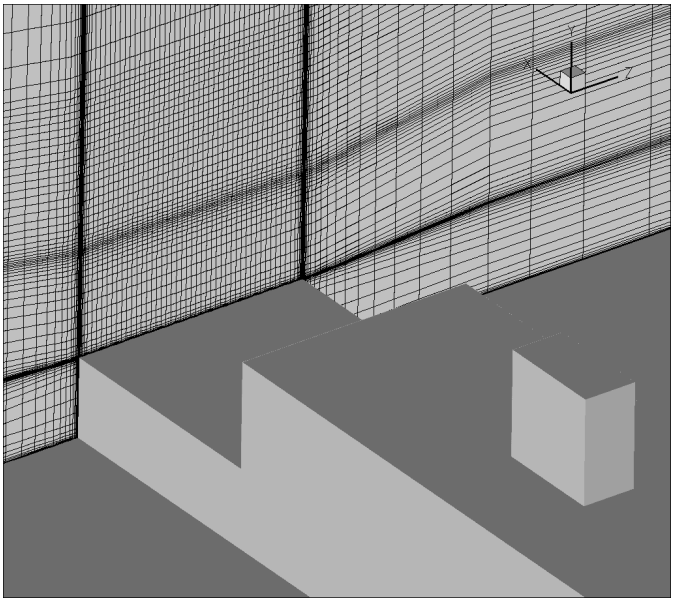

(f) Slice of Volume Mesh in X-direction

Figure 1: Surface blocking and mesh for the SFS2 geometry.

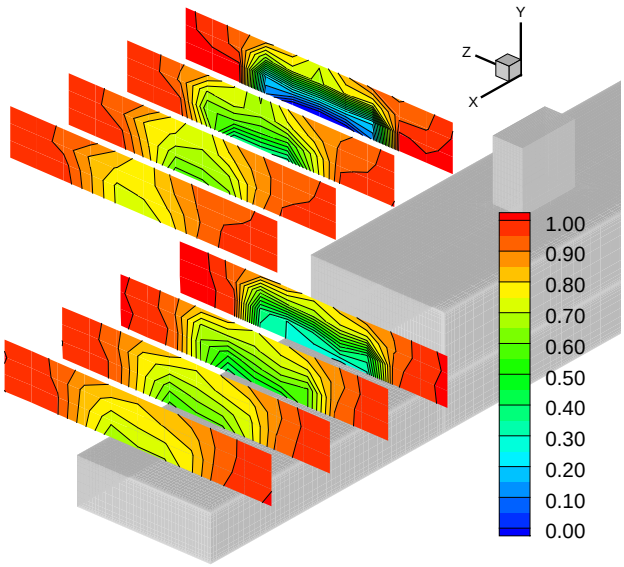

(a) Mean Streamwise Velocity

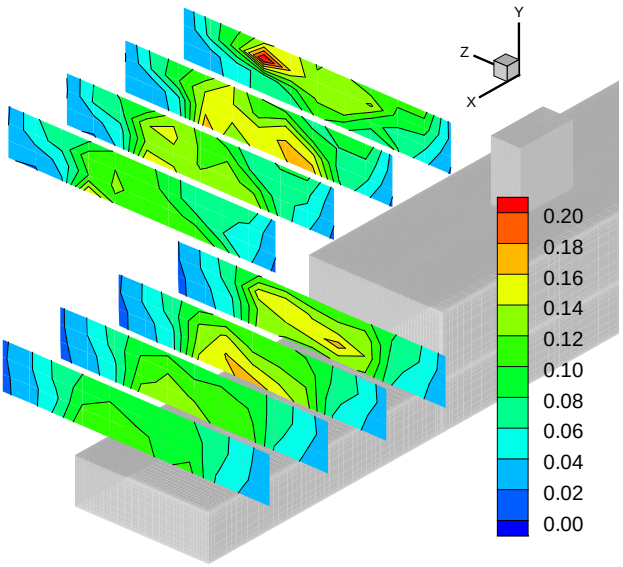

(b) RMS Streamwise Velocity

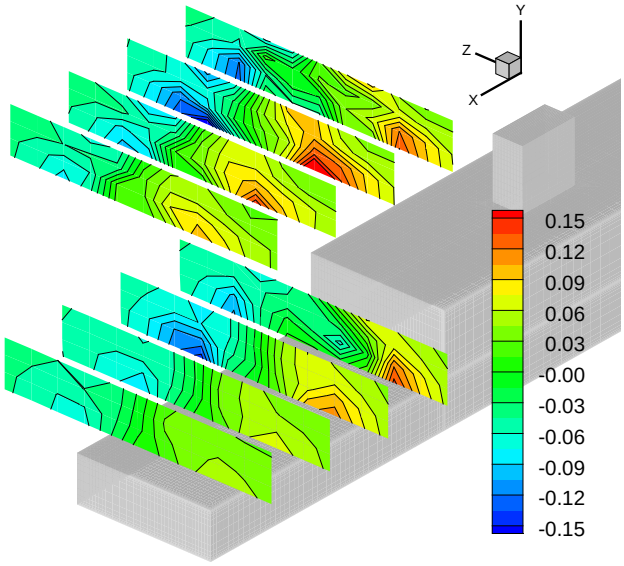

(c) Mean Spanwise Velocity

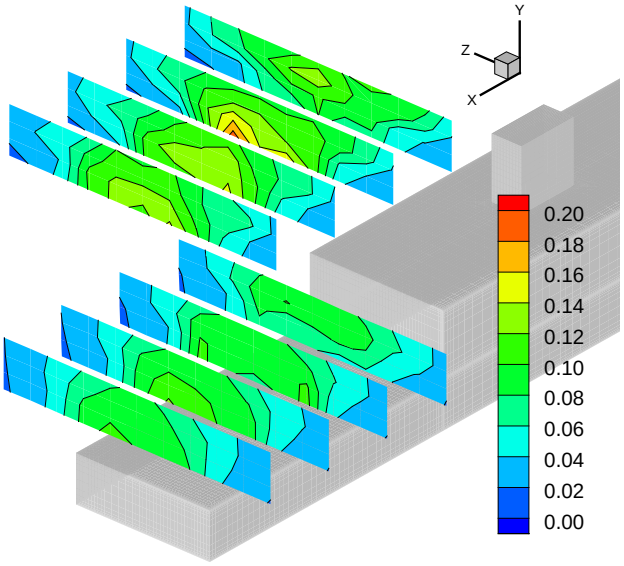

(d) RMS Spanwise Velocity

Figure 2: Mean and RMS velocities for the headwind test case using the DES S-A turbulence model.

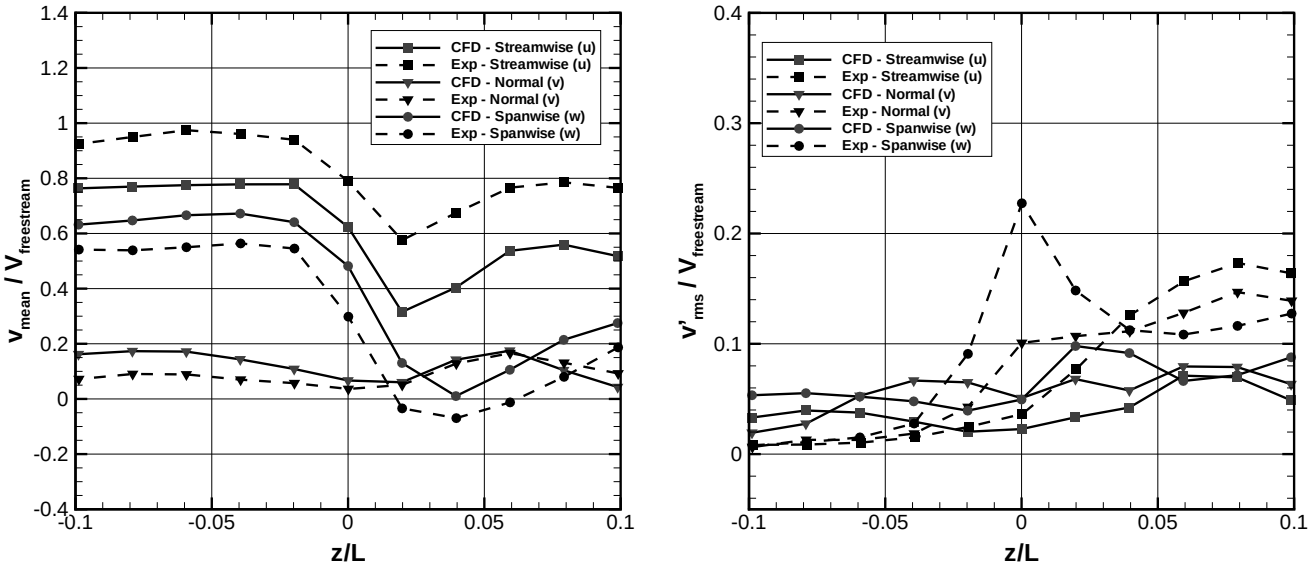

(a) URANS

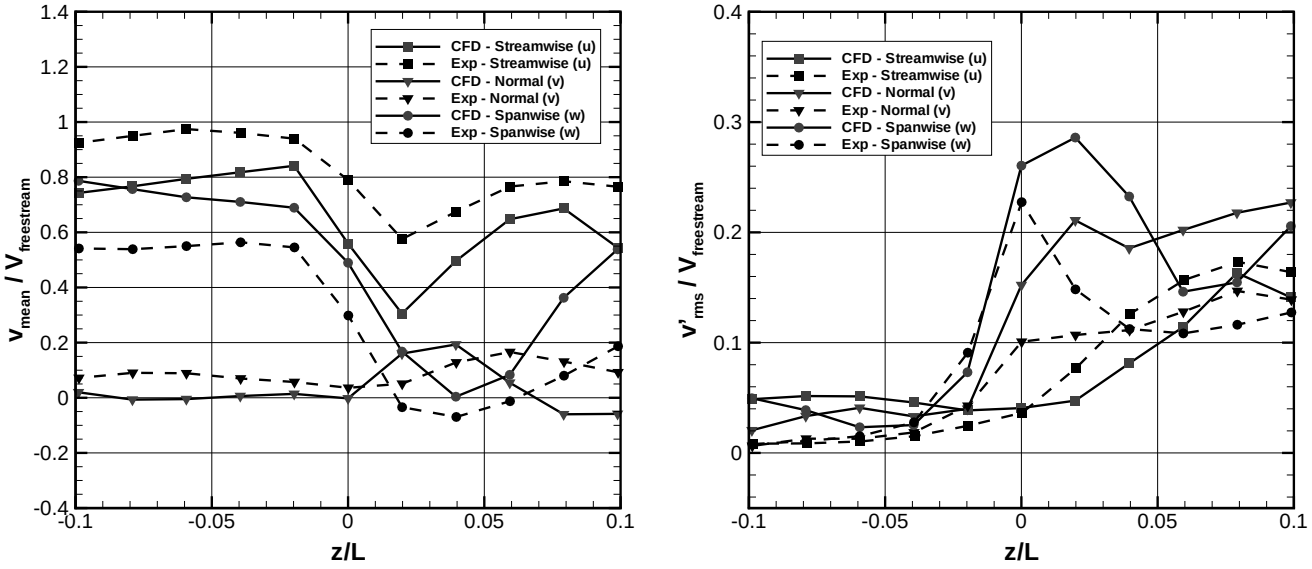

(b) DES

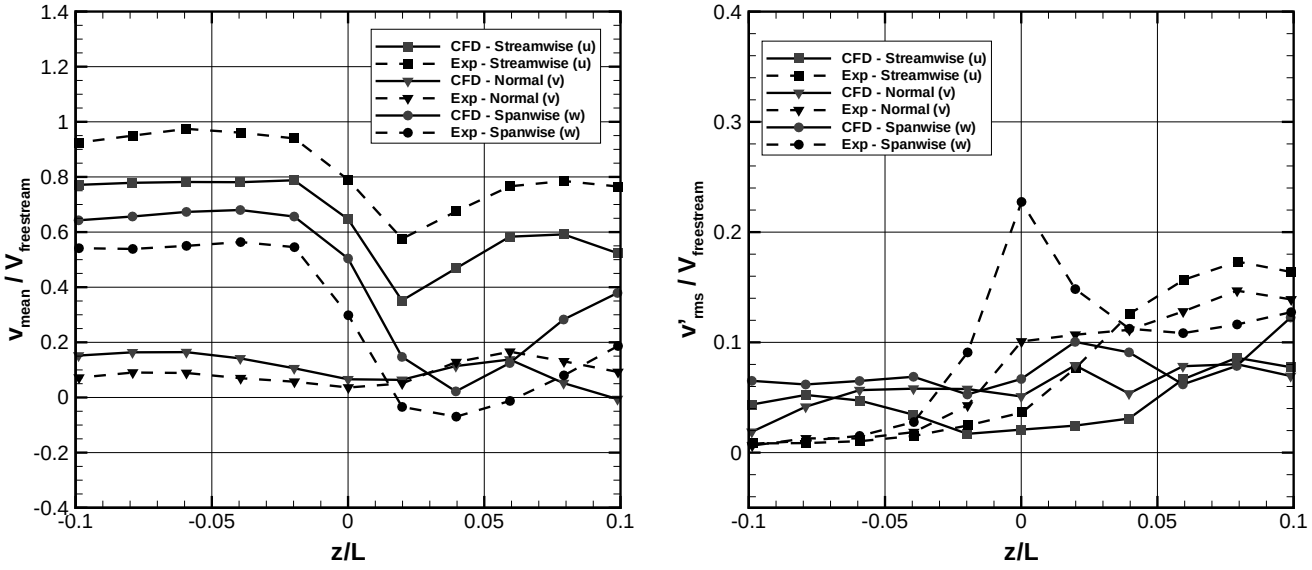

(c) DDES

Figure 3: Mean and RMS plots at 50% deck length for the 45 degrees wind test case using the S-A URANS and DES models.

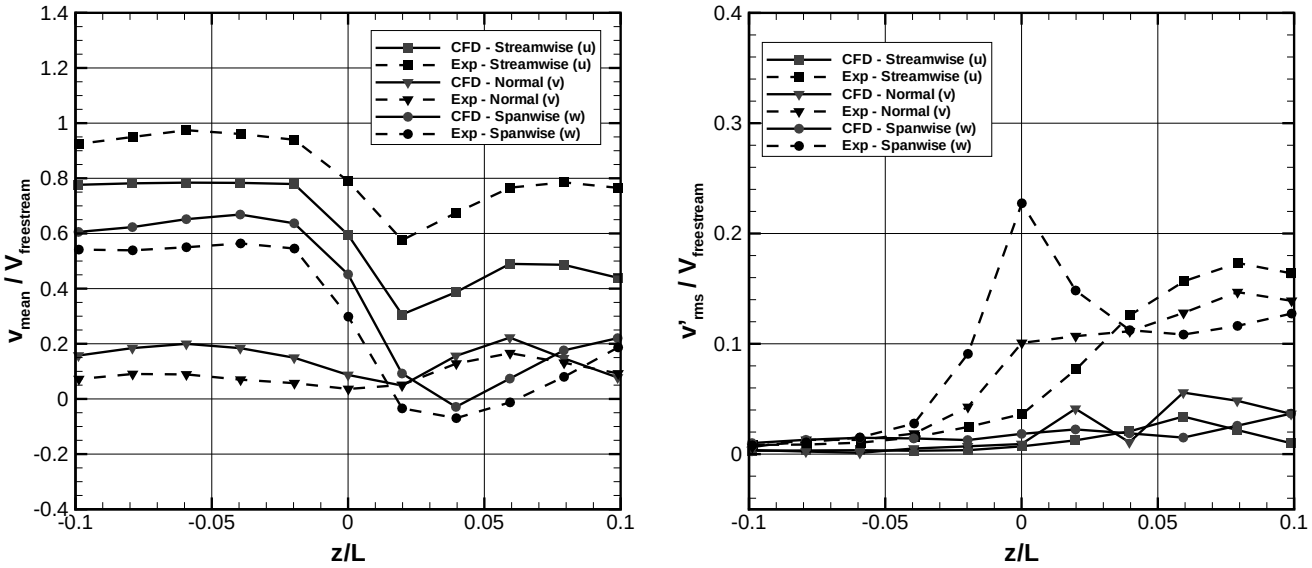

(a) URANS

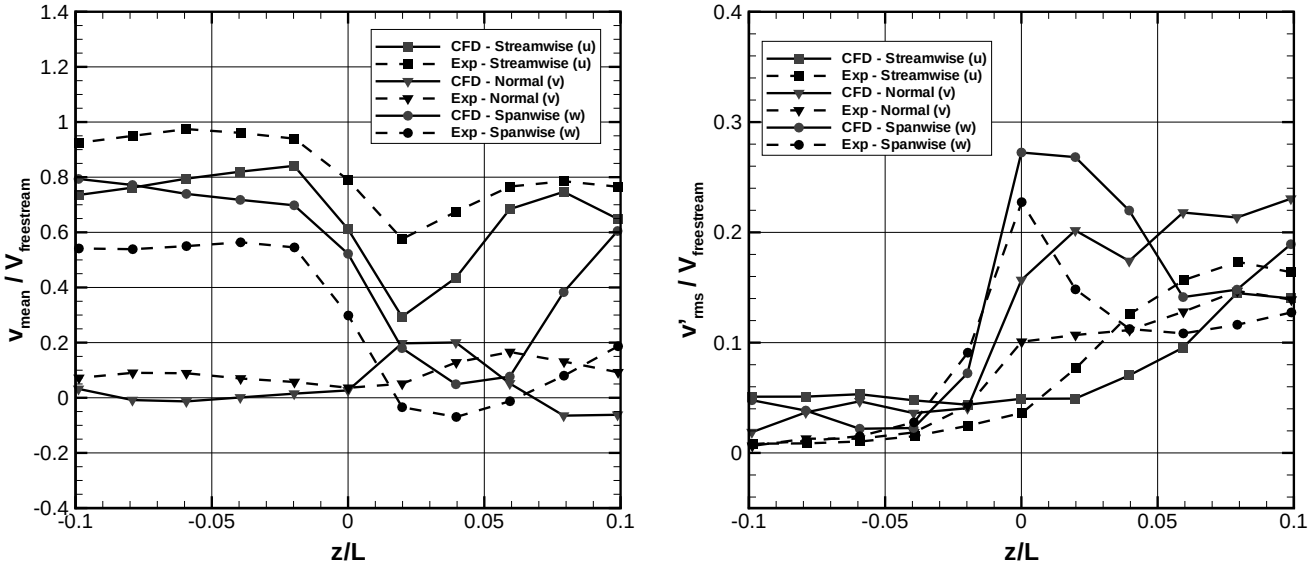

(b) DES

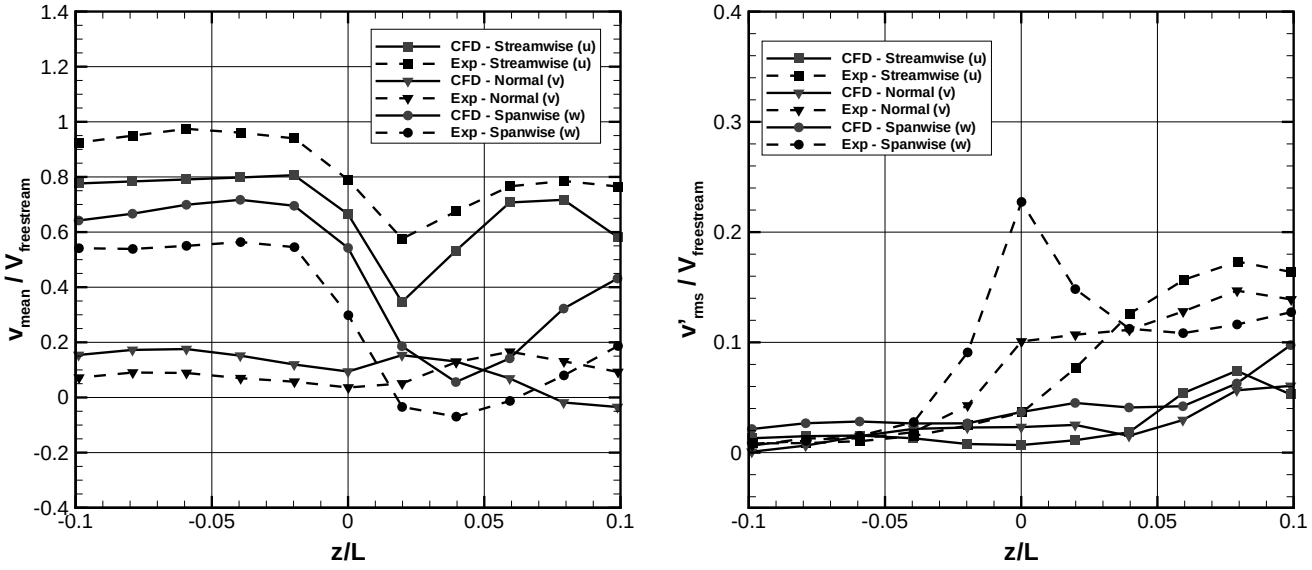

(c) DDES

Figure 4: Mean and RMS plots at 50% deck length for the 45 degrees wind test case using the SALSA URANS and DES models.

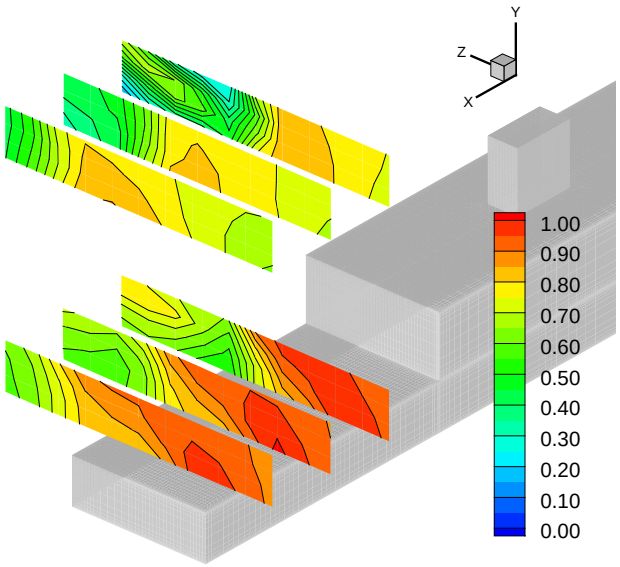

(a) Mean Streamwise Velocity

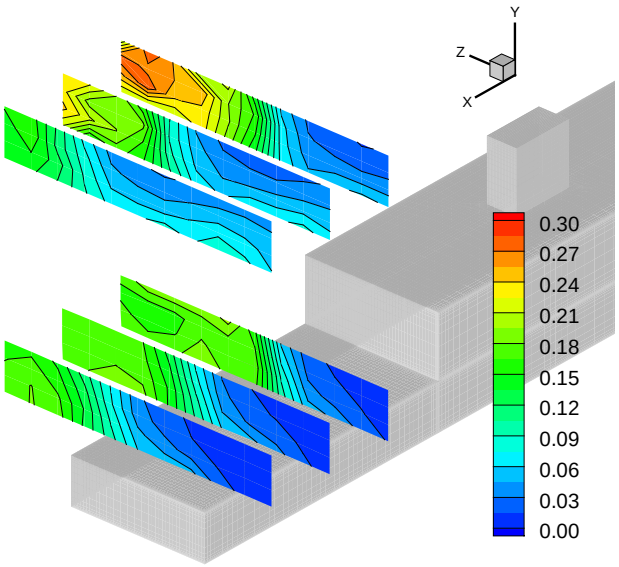

(b) RMS Streamwise Velocity

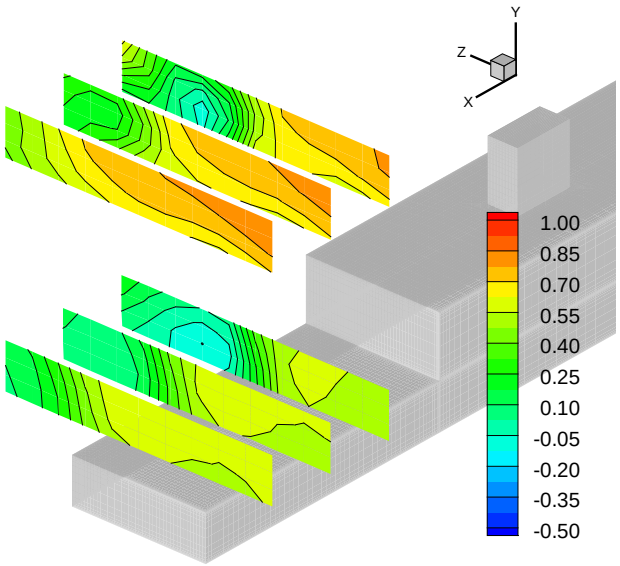

(c) Mean Spanwise Velocity

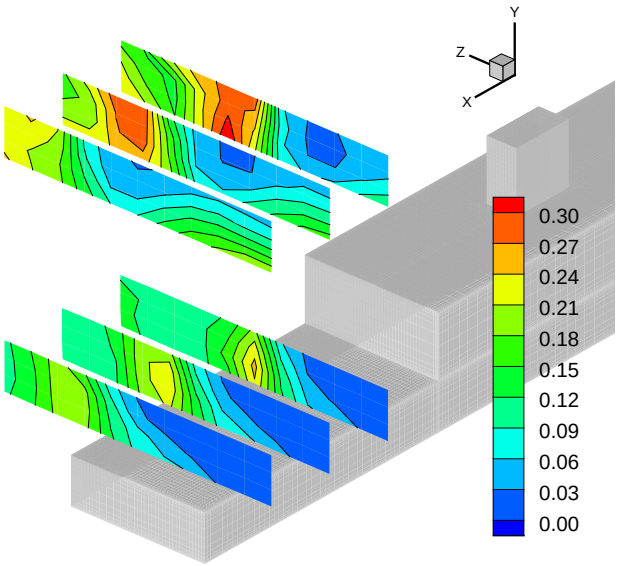

(d) RMS Spanwise Velocity

Figure 5: Mean and RMS velocities for the 45 degrees wind test case using the DES S-A turbulence model. Upper maps are CFD results, lower maps are experimental data

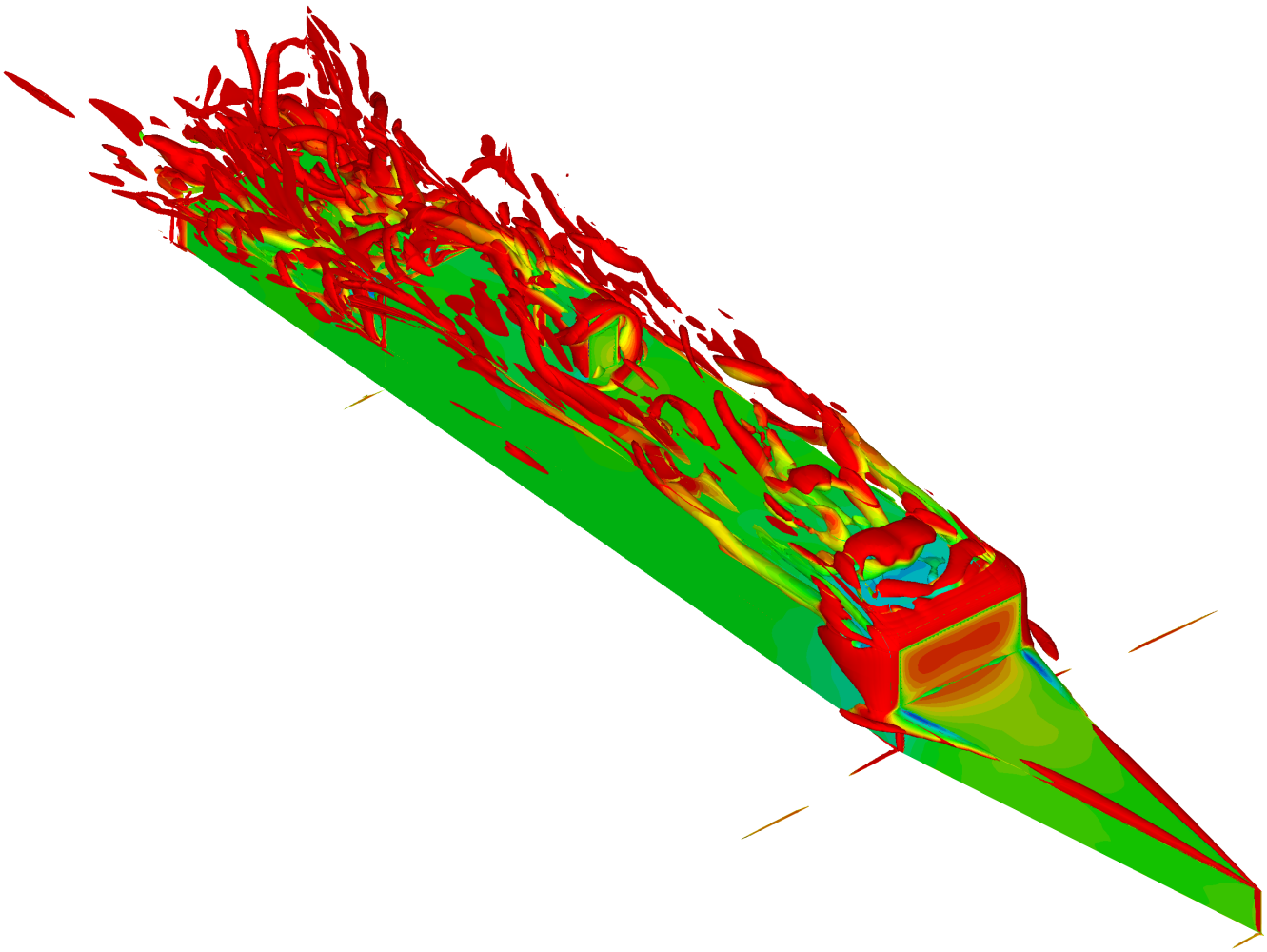

(a) Whole Domain

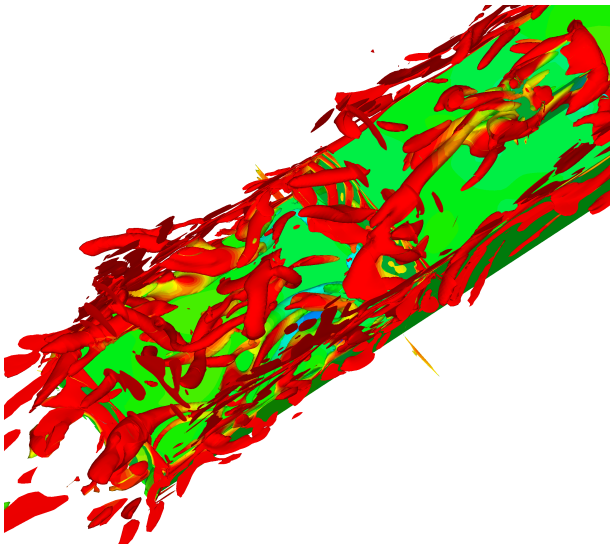

(b) Ship's Landing Deck

Figure 6: Iso-surfaces of Q-Criteria for the headwind test case using the DES S-A turbulence model. Iso-surfaces are at a levle of Q=5000 and coloured with streamwise velocity. Ship surface is coloured with surface pressure contours.

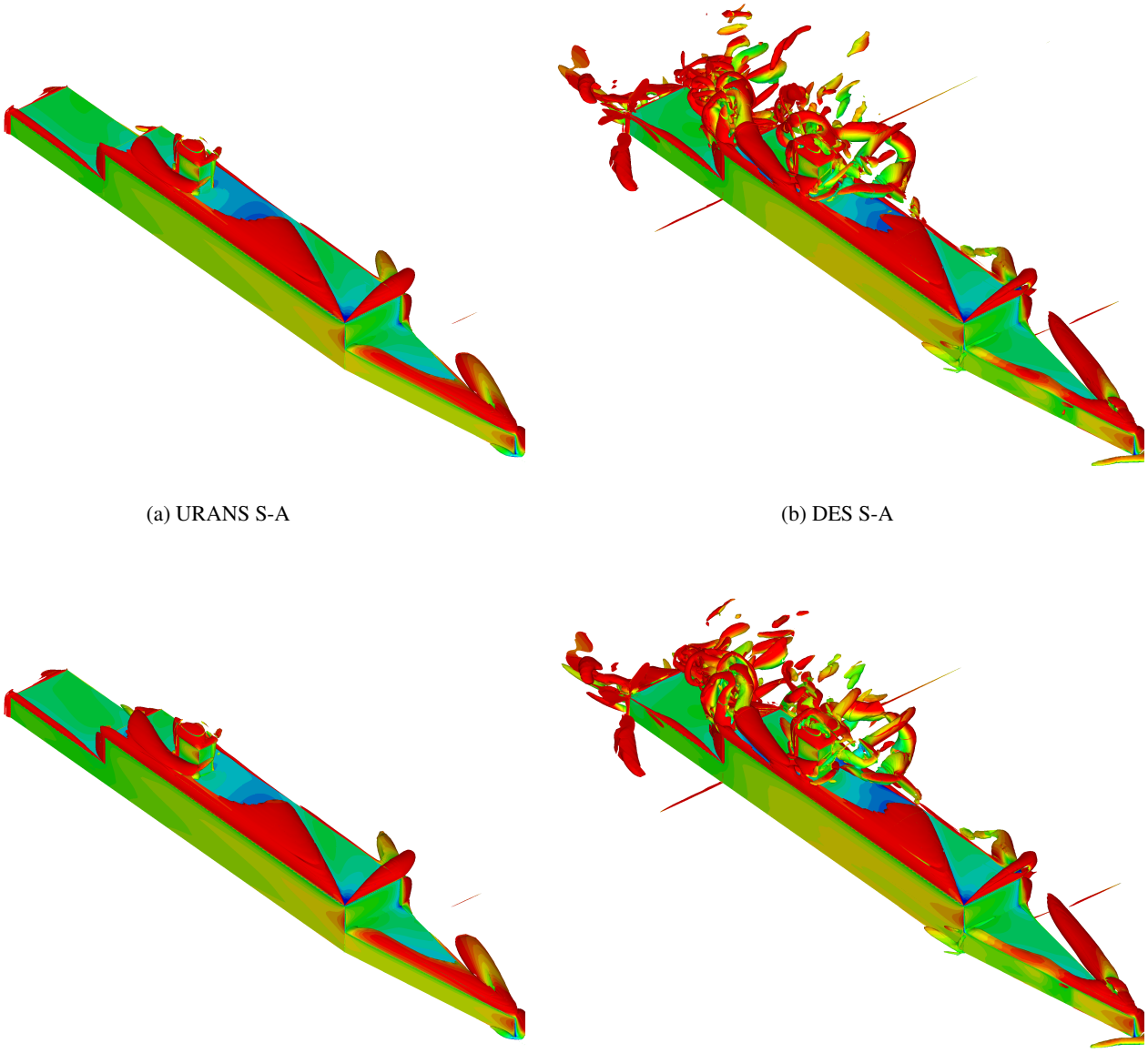

(a) URANS S-A

(b) DES S-A

(c) DDES S-A

(d) DES SALSA

Figure 7: Iso-surfaces of Q-Criteria for the 45 degrees wind test case. Iso-surfaces are at a levle of Q=5000 and coloured with streamwise velocity. Ship surface is coloured with surface pressure contours.

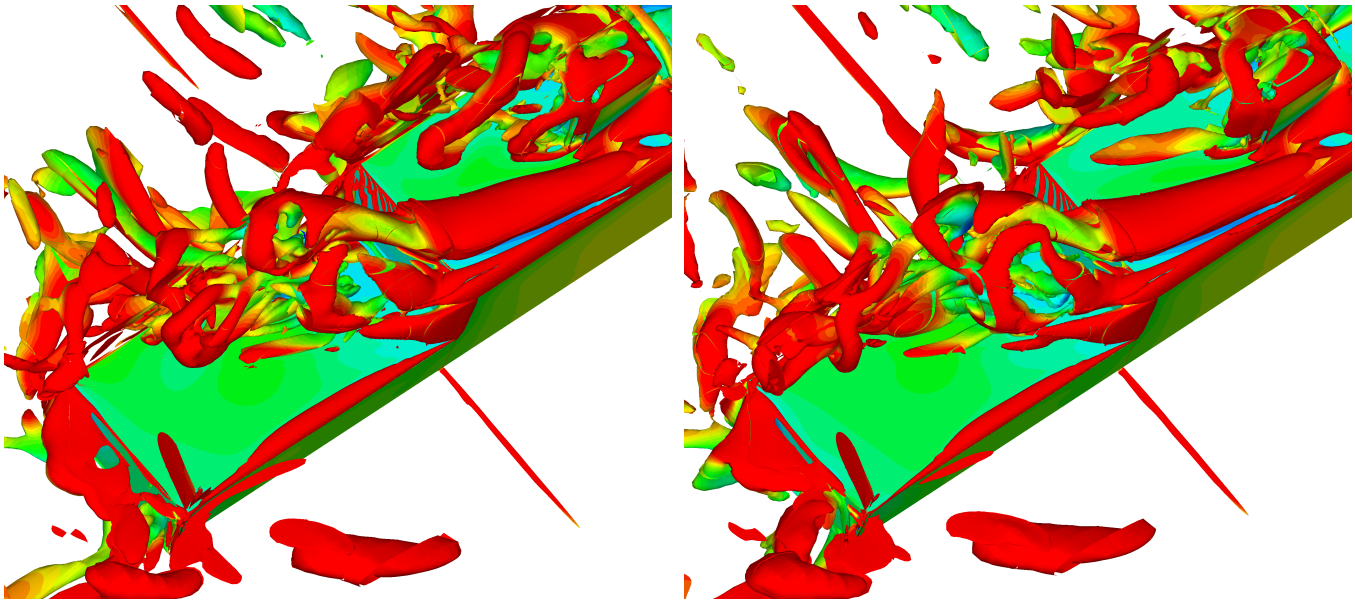

(a) DES S-A (b) DES SALSA

Figure 8: Iso-surfaces of Q-Criteria over the ship's landing deck for the 45 degrees wind test case. Iso-surfaces are at a levle of Q=5000 and coloured with streamwise velocity. Ship surface is coloured with surface pressure contours.

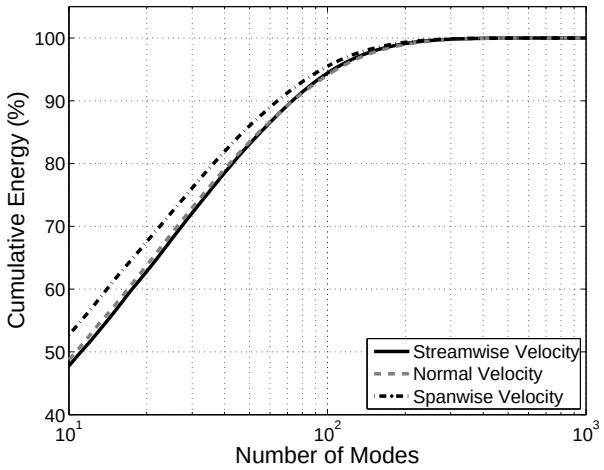

Figure 9: Cumulative energy for an increasing number of the POD modes.

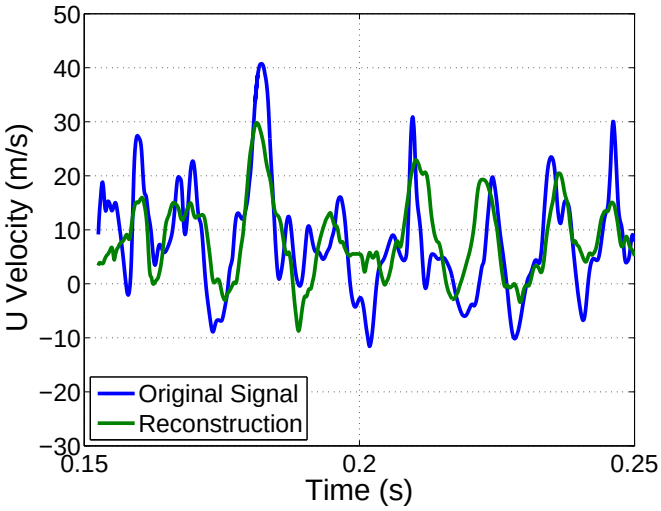

(a) 10 Modes - Streamwise Velocity

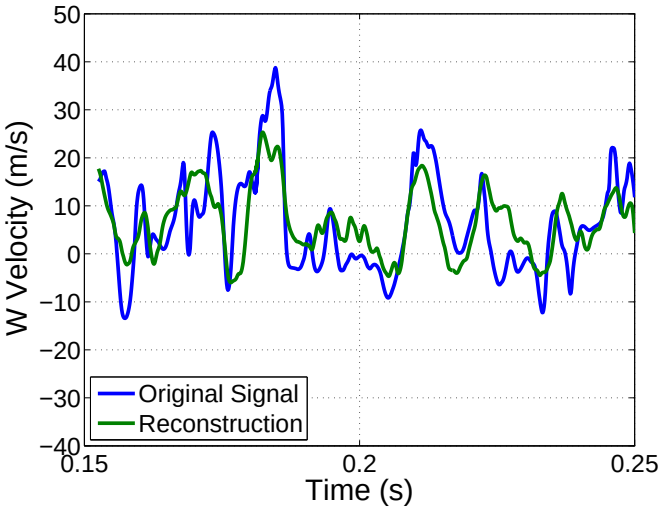

(b) 10 Modes - Spanwise Velocity

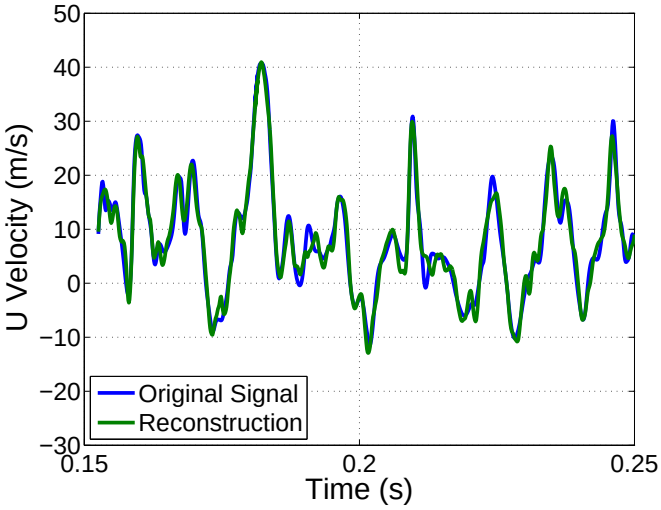

(c) 100 Modes - Streamwise Velocity

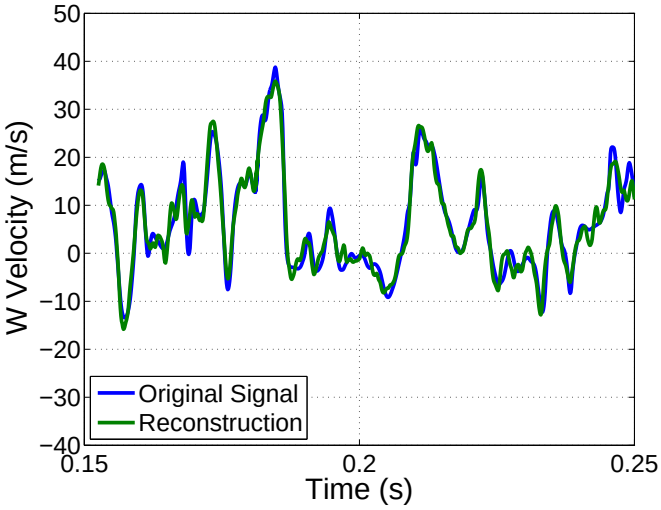

(d) 100 Modes - Spanwise Velocity

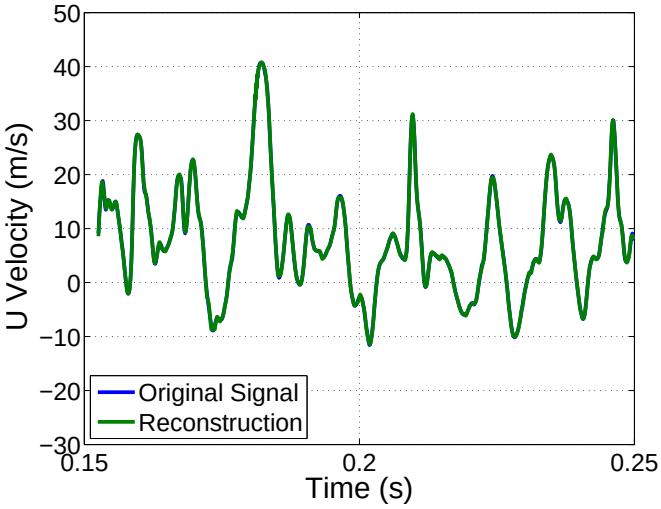

(e) 350 Modes - Streamwise Velocity

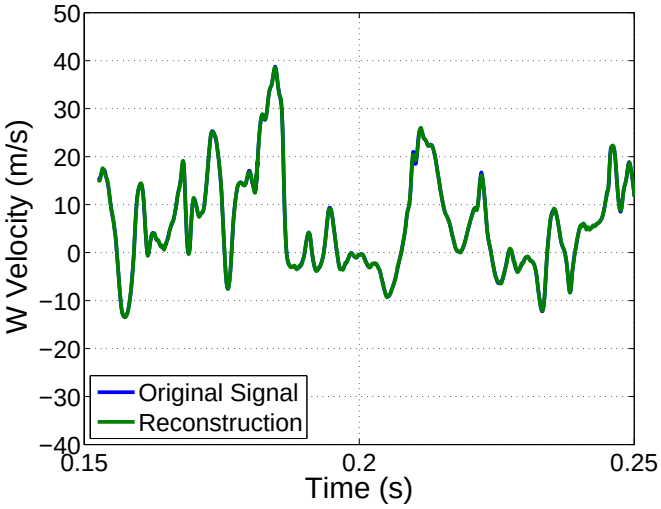

(f) 350 Modes - Spanwise Velocity

Figure 10: Reconstructions of the streamwise and spanwsie velocity signal using increasing modes.

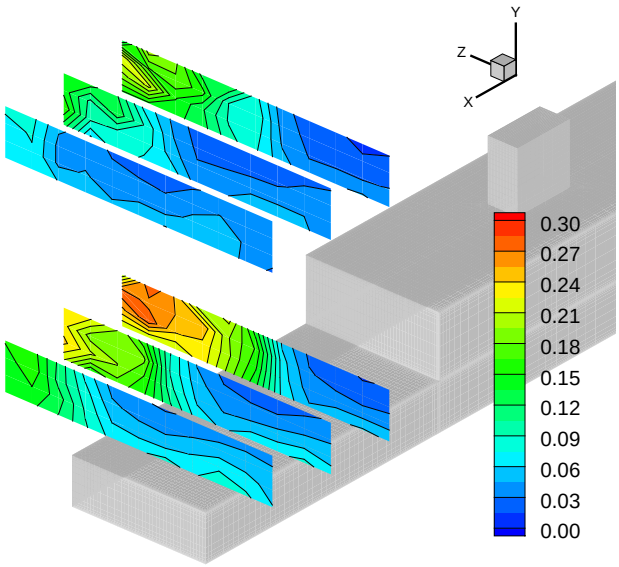

(a) RMS Streamwise Velocity: 10 Modes

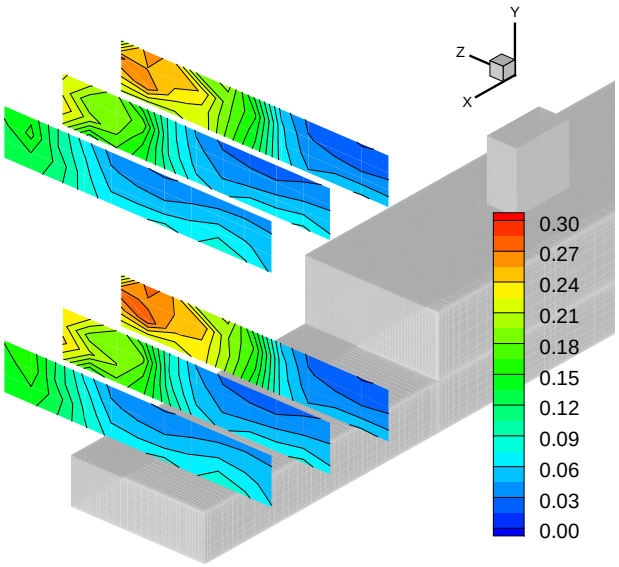

(b) RMS Streamwise Velocity: 100 Modes

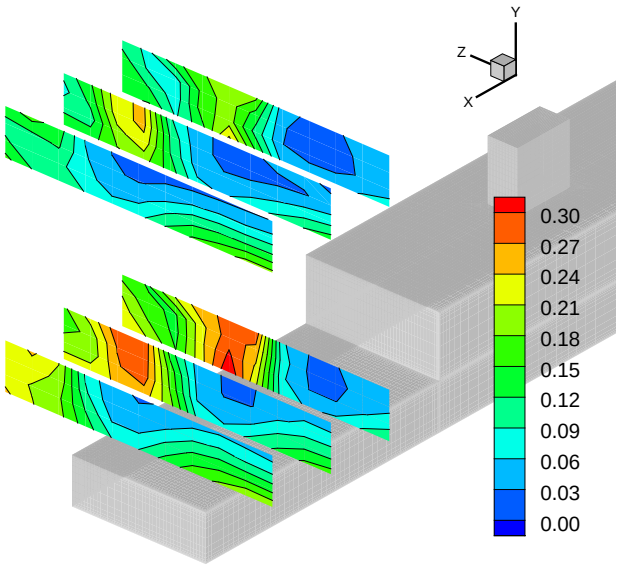

(c) RMS Spanwise Velocity: 10 Modes

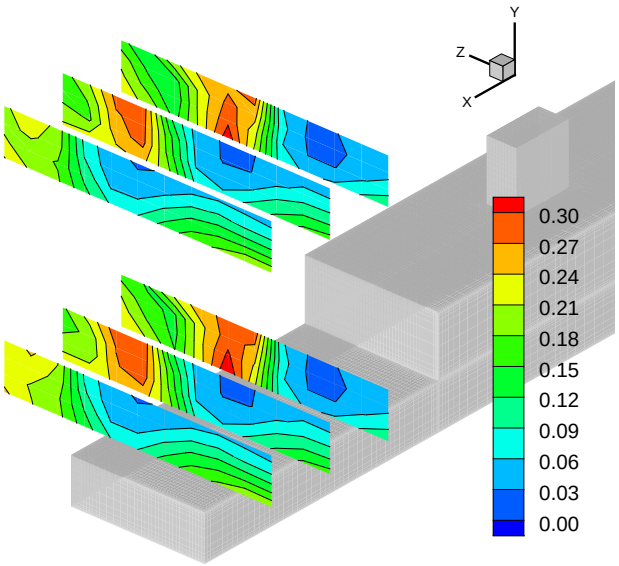

(d) RMS Spanwise Velocity: 100 Modes

Figure 11: RMS velocities for reconstructions of the 45 degrees wind test case using 10 and 100 modes. Lower maps are original CFD results, upper maps are the reconstructions.

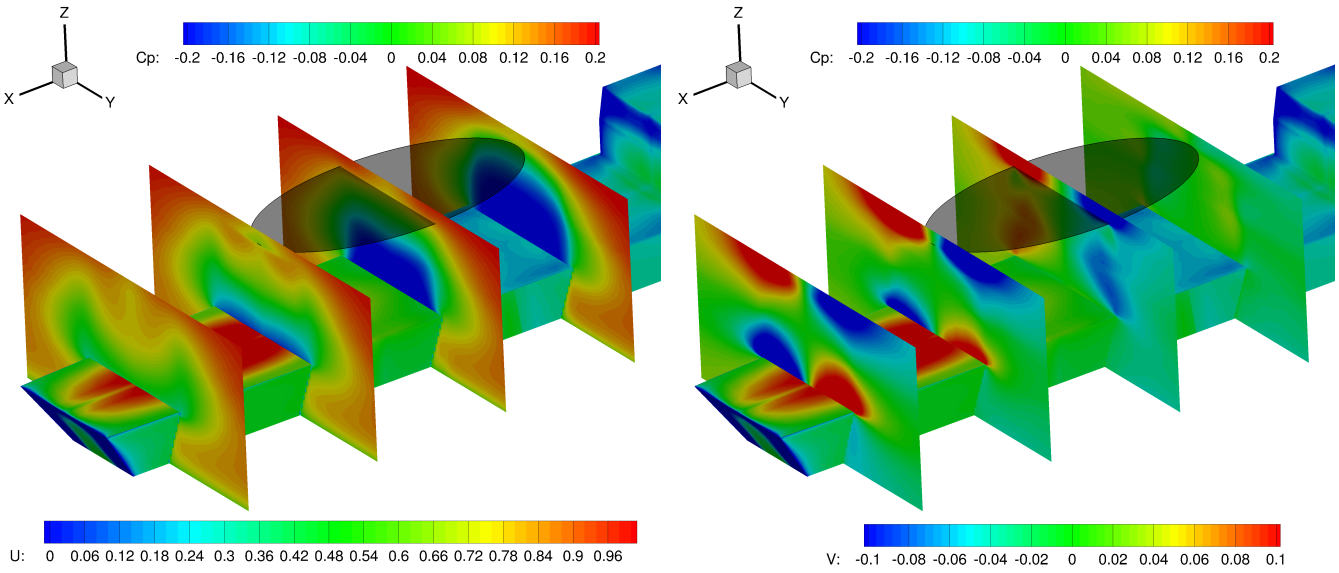

Figure 12: Maps of streamwise and spanwise velocities adimensionalized by the freestream streamwise velocity and pressure coefficient on the ship surface, with actuator disc. The streamwise axis is scaled by 2 for clarity, the shaded circle gives the position of the actuator disc. $C_T^{UK} = 0.00734$, $\mu = 0.118$, $h = 9m$, Wind angle = 0°

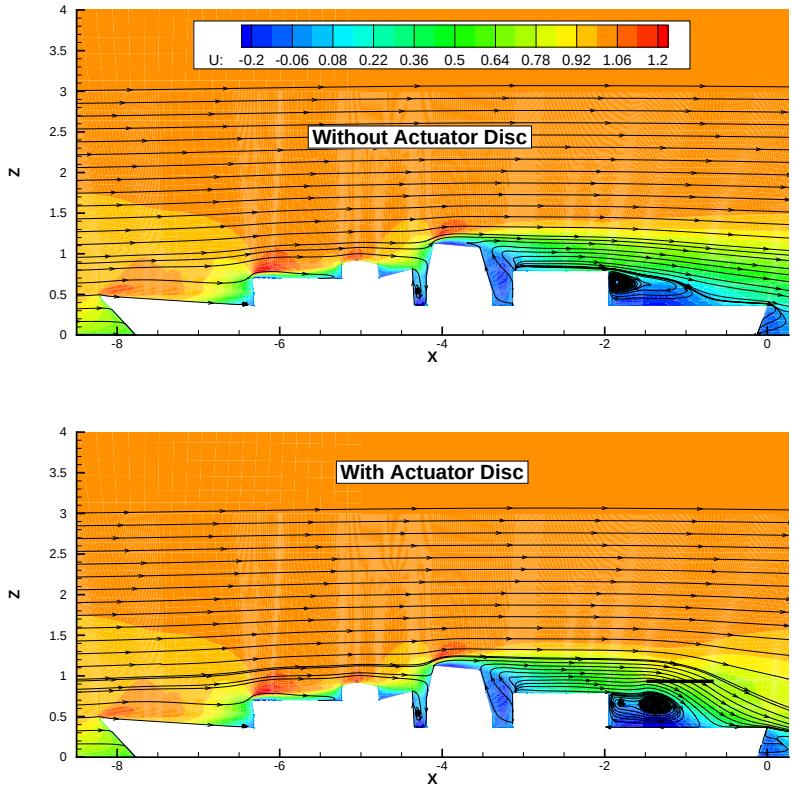

Figure 13: Streamwise velocity and streamlines, with and without actuator disc. $C_T^{UK} = 0.00734$, $\mu = 0.118$, $h = 9m$, Wind angle = 0°

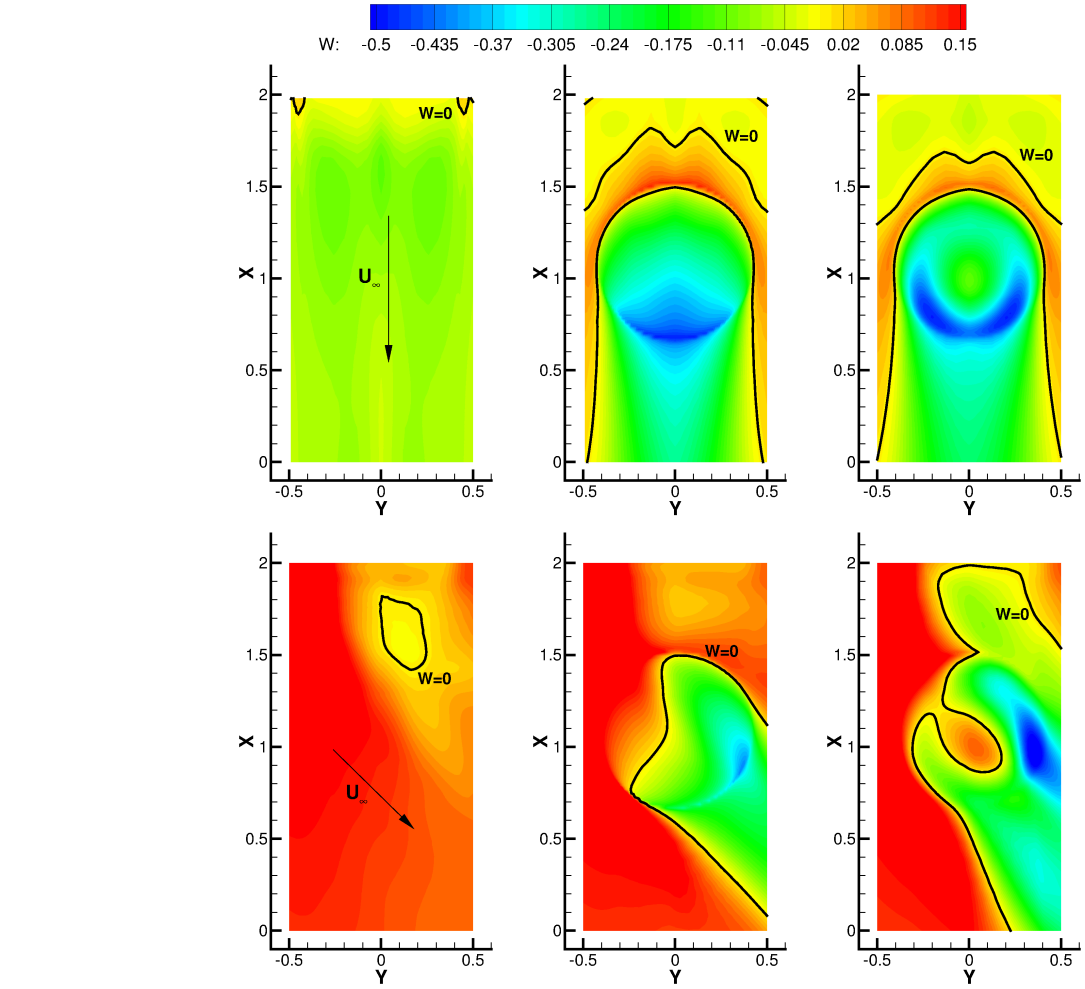

Figure 14: Comparison of downwash velocity (W) components above the deck without actuator disc (Left) and with uniform (Middle) and non-uniform (Right) actuator discs for wind directions of $0°$ (Upper) and $Red - 45°$ (Lower).

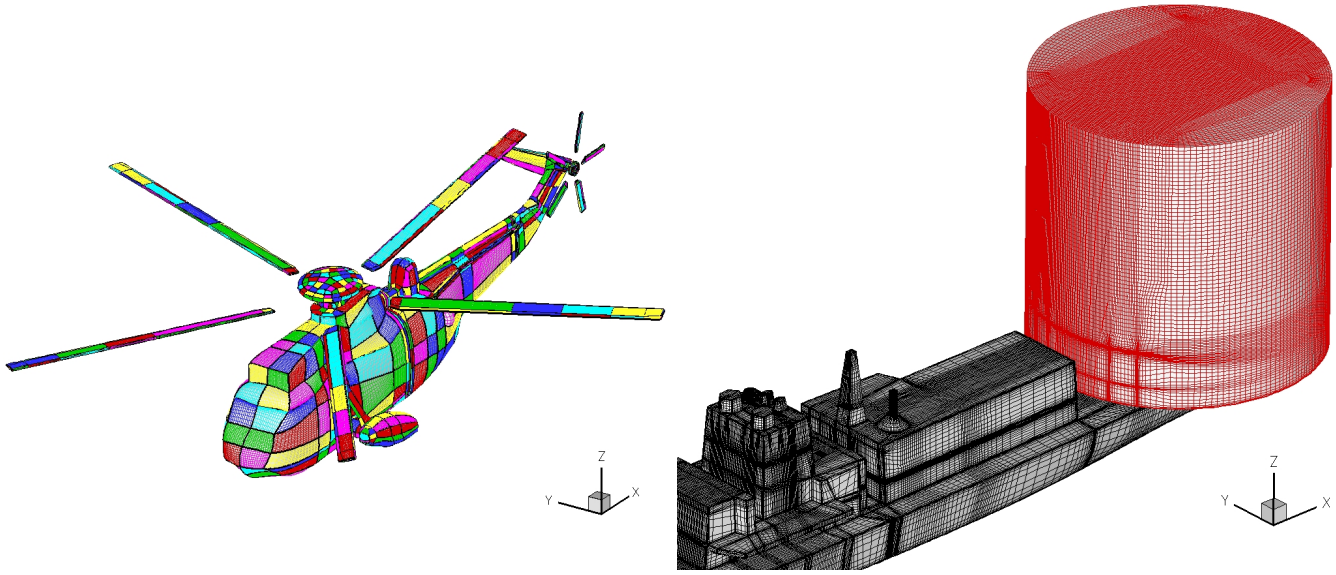

Figure 15: Views of the Sea-King and Type-23 frigate grids used in this study. The drum in red shows the sliding planes that separate the Sea-King grid from the Type-23.

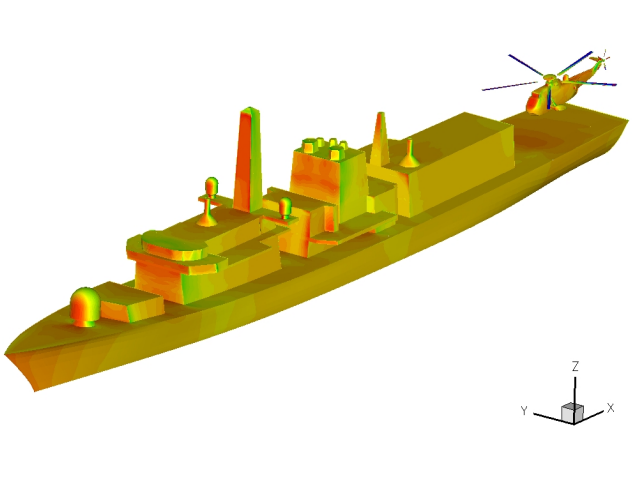

(a) Frigate and Sea King

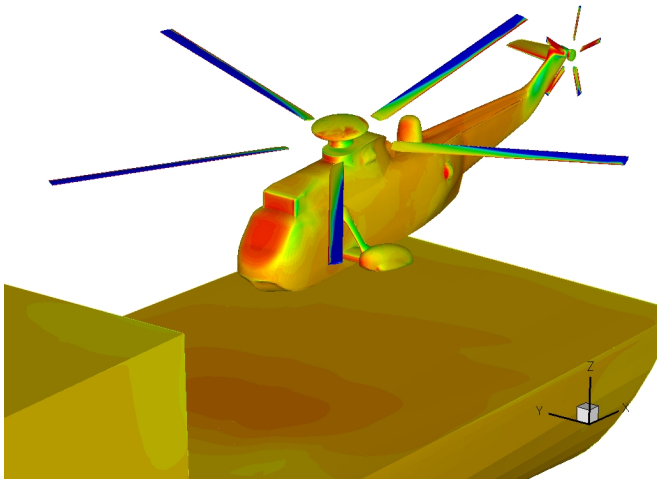

(b) Sea King

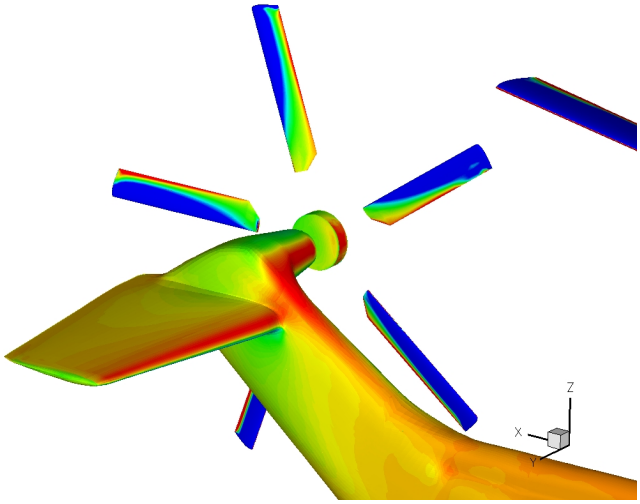

(c) Tail Rotor

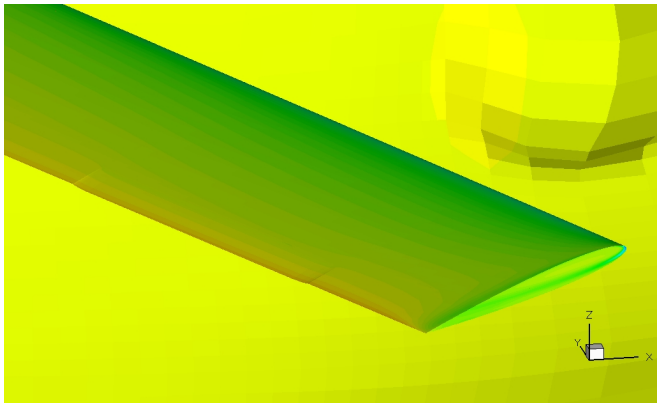

(d) Active Flaps on Main Rotor

Figure 16: Sea King and T23 Frigate Computation

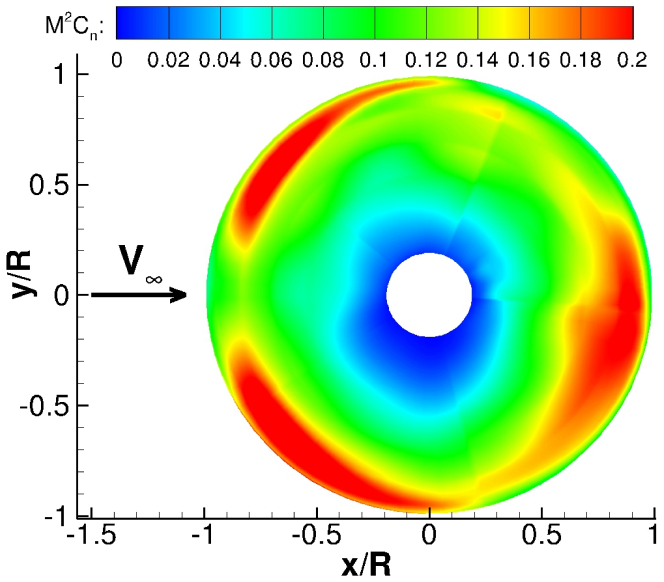

(a) Normal Force

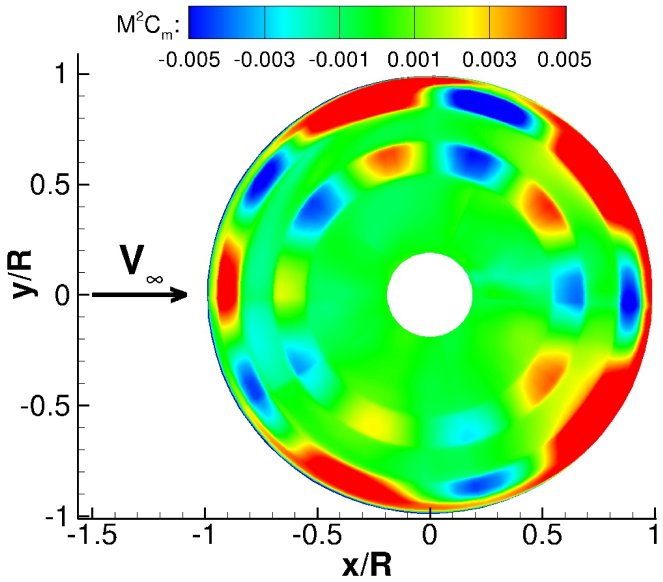

(b) Blade Pitching Moment

Figure 17: Loads on the rotor of the Sea King helicopter inside the wake of the ship.